N73 - 23914

CR - 128911

STUDY OF AN EXPERIMENTAL
TECHNIQUE FOR APPLICATION TO
STRUCTURAL DYNAMIC PROBLEMS

MARCH 1973

McDonnell Douglas Astronautics Company

STUDY OF AN EXPERIMENTAL
TECHNIQUE FOR APPLICATION TO
STRUCTURAL DYNAMIC PROBLEMS

MARCH 1973

R. F. SNELL

APPROVED BY:

J. F. Garibotti

J. F. GARIBOTTI
ACTING CHIEF ADVANCE TECHNOLOGY ENGINEER
STRUCTURES AND MECHANICAL DEPARTMENT
RESEARCH AND DEVELOPMENT
ADVANCE SYSTEMS AND TECHNOLOGY

McDonnell Douglas Astronautics Company

ABSTRACT

An experimental program was conducted to determine the feasibility of using subscale Lexan plastic models to determine the response of full-scale aerospace structural components to impulsive, pyrotechnic loadings. A Lexan monocoque cylinder was impulsively loaded around the circumference of one end, causing a compressive stress wave to propagate in the axial direction. The resulting structural responses of two configurations of the cylinder (with and without a cutout) were recorded by photoelasticity, strain gages, and accelerometers. A maximum dynamic stress concentration was photoelastically determined and the accelerations calculated from strain-gage data were in good agreement with those recorded by accelerometers. On the basis of results from these tests, it is concluded that reliable, quantitative structural response data can be obtained by the experimental techniques described in this report.

In addition to being able to obtain quantitative data for the structural response of the Lexan model, it is essential to have similitude relations, by means of which, (a) a subscale model can be properly designed, and (b) the response of the prototype can be related to the response of the model. Exact similitude relations were obtained for elastic materials and for two different classes of viscoelastic materials.

The central conclusion is that the use of subscale Lexan models to determine the structural response of impulsively loaded aerospace structural components is feasible, subject only to the usual limitations encountered in all model testing. The potential cost reduction afforded by reliable subscale testing make the development of this technique highly desirable.

FOREWORD

The work described in this report was conducted under NASA Contract NAS9-12873 and the Program Monitor was D. K. McCutchen, Structures Branch, NASA-MSC.

A special note of acknowledgement is due Dr. E. L. Stanton who conducted the similitude study described in this report.

TABLE OF CONTENTS

LIST OF TABLES

LIST OF FIGURES

LIST OF FIGURES (Continued)

LIST OF SYMBOLS

A_M	Maximum acceleration (L/T^2)
A_X	Acceleration in X direction (L/T^2)
c_o	Propagation velocity (L/T)
$C_{ijk\ell}$	Elastic response coefficients (F/L^2)
$C^1_{ijk\ell}$	Viscoelastic response functions (F/L^2)
d	Material thickness (L)
d_i	Direction cosines of the gravitational field
E	Young's modulus (F/L^2)
e	Dilatation
f_i	Body force (F/L^3)
f^*_i	Nondimensional body force
g	Acceleration of gravity (32 ft/sec^2) (L/T^2)
g^*	Nondimensional acceleration of gravity
K	Stress optical coefficient (F/L)
ℓ	Characteristic length (L)
m	Subscript designating model
n	Fringe order
P	Strain duration (T)
p	Subscript designating prototype
S_i	Surface tractions (F/L^2)
t	Time (T)
u_i	Displacement components (L)
u^*_i	Nondimensional displacement components
v_X	Velocity in X direction (L/T)
x	X coordinate (L)
z_i	Coordinates (L)

α Dummy variable of integration

δ_{ij} Kronecker delta; equal to 1 for i=j, equal to 0 for i≠j

ϵ_M Maximum strain

ϵ_x Strain in X direction

ϵ_{ij} Strain components

$\dot{\epsilon}$ Derivative of strain with respect to time (1/T)

η Strain rate parameter (FT/L^2)

λ Lamé constant (F/L^2)

$\lambda^1(t)$ Viscoelastic response function (F/L^2)

μ Lamé constant (F/L^2)

$\mu^1(t)$ Viscoelastic response function (F/L^2)

ν Poisson's ratio

ξ_i Nondimensional coordinates

ρ Density (FT^2/L^4)

σ_x Stress in X direction (F/L^2)

σ_y Stress in Y direction (F/L^2)

σ_{ij} Stress components (F/L^2)

τ Nondimensional time

1   Subscript designating mount

2   Subscript designating cylinder

Symbols in parentheses indicate units; F for force, L for length, and T for time.

Tensorial indices are designated by lower-case Latin letters, and range over the values 1 to 3. The summation convention is used wherever tensorial indices are repeated. Thus, the quantity $\dfrac{\partial \sigma_{ij}}{\partial z_j}$ is understood to be equal to $\sum\limits_{j=1}^{3} \dfrac{\partial \sigma_{ij}}{\partial z_j}$.

INTRODUCTION AND SUMMARY

Pyrotechnic devices are commonly used today in space vehicles for several purposes, e.g., stage separation, bay removal, and fairing removal. The detonation of these devices imparts shock loading to the vehicle structure and to the components attached to this structure. For a given application, the pyrotechnic devices must be designed in conjunction with the vehicle structure and components such that the integrity of the vehicle and its mission are not compromised by the shock loading. Unfortunately, limited information is available to the designer on shock levels generated from pyrotechnic detonations and on the effects that these shock loadings have on the vehicle structure and components. This condition exists for two reasons. First, stress-wave propagation and interaction that result from shock loadings are extremely complicated physical phenomena. Consequently, analytical solutions to such phenomena are difficult, even for the simplest of cases, and are infeasible in most instances for actual problems. Second, experimental data on shock loading and on the response of vehicles to shock loadings are limited because of the limited amount of testing that has been conducted. This limitation is primarily a result of the large costs associated with full-scale, destructive pyrotechnic testing. This latter problem is further compounded by the fact that past experimental test results, by their very nature, are directly applicable only to the actual hardware tested. The use of these results for the design of future vehicles must rely on extrapolation of data to configurations that are often only remotely similar to the configurations that yielded the data. In such situations it is not surprising that predictions of response are often erroneous.

The above considerations underscore the need both for more powerful analytical techniques and for less expensive, more versatile experimental techniques for investigating shock loading and the response of structures to shock loading. McDonnell Douglas Astronautics Company (MDAC), under the sponsorship of NASA Contract NAS9-12873, conducted an experimental program to investigate the feasibility of one improved experimental technique, that of an electromagnetic, stress-wave generator augmented by dynamic photoelastic, strain-gage, and accelerometer instrumentation techniques for the determination of dynamic response in models of proposed vehicles.

This technique can be divided into three areas, that of the loading device, that of the model, and that of instrumentation for determination of the response of the model to the loading. The loading device employs the energy stored in a high-energy, high-voltage capacitor bank to produce uniform impulsive loads that simulate shock loads from the detonation of pyrotechnic devices. The test specimen models proposed vehicle configurations and is made of Lexan polycarbonate plastic. Lexan, a photoelastic material, allows the determination of the states of strain in the model by use of a dynamic polariscope. The model can also be instrumented with strain-gages and low-mass accelerometers to further characterize the model response. As a final step in this technique, the dynamic response of the model must be related to the dynamic response of an actual prototype by the use of appropriate similitude relationships.

This experimental technique has two principal advantages. First, because the technique is relatively inexpensive in comparison to full-scale pyrotechnic testing of actual hardware, this technique would allow the determination of the dynamic response of proposed configurations early in the design stages. If the tests indicated that these proposed configurations were inadequate, redesign could be initiated before production of the actual hardware. This technique would also allow the conduction of parametric studies for determination of a satisfactory configuration if early tests indicated that the original designs were inadequate.

The second principal advantage is that the technique would allow the determination of the states of strain in the model. Consequently, the testing of a model of a hardware configuration which had previously demonstrated failure in actual pyrotechnic tests would allow the determination of the failure mechanisms. This is in contrast to the information normally available from actual hardware tests in that results from hardware tests are generally limited to determining if the part does or does not fail under shock loading.

In the study performed under the NASA contract, MDAC investigated the feasibility of such a technique, using the available MDAC stress-wave generator to conduct three test series on two configurations (without a cutout and with a cutout) of a simple monocoque cylinder of Lexan. In these tests the generator loaded the cylinder in the axial direction around the circumference of the cylinder such that a compressive stress wave propagated in the axial direction of the cylinder. The stress wave had a sine-squared shape with a duration of approximately 25 microseconds and produced a peak strain in the cylinder of approximately 5500 μ in/in. A dynamic photoelastic polariscope and strain gages were used to determine the states of strain in the cylinder and accelerometers were also used to obtain data for correlation with the photoelastic and strain-gage data. As the thickness of the walls of the model were inadequate to allow the installation of the accelerometers directly to the model, the accelerometers were attached to a Lexan block which, in turn, was attached to the walls of the cylinder. The experimental data was analyzed to determine dynamic response of the model (acceleration and shock spectra) and finally a study was conducted to investigate problems associated with the scaling of model results in the determination of the dynamic response of an actual prototype.

Reduction of the data indicated excellent correlation between the strain-gage and accelerometer results (4 percent difference) and good correlation between the photoelastic and accelerometer results (14 percent difference). For both comparisons accelerometer data were compensated to account for the effects of the accelerometer mounting block. The scaling study showed that, for models and prototypes made of linear elastic materials and loaded in the elastic range at load rates below 10^3 in/in/sec., all required scaling relationships can be satisfied with the exceptions of the relationships involving body forces and the relationships involving Poisson's ratio. Body forces can in all likelihood be neglected but the effects of incompatibility of Poisson's ratio must be assessed with analytical and experimental means. In the event such effects are unacceptable and uncompensatible, models must be constructed

from the same materials as the prototype. Scaling relationships were also developed for two classes of viscoelastic materials. The scaling study showed that the relationships of one of these classes can be satisfied even at load rates greater than 10^3 in/in/sec. The results of the scaling study in conjunction with the excellent data correlations show that the modeling techniques investigated in this program may indeed be feasible for predicting the response of full-scale prototypes to pyrotechnic shock loads.

MODEL DESCRIPTION

A cylinder of Lexan polycarbonate plastic was fabricated to the dimensions shown in Figure 1. These dimensions were chosen for a number of reasons. First, an inside diameter of 10.66 inches was established to allow the use of an existing forming mandrel, thereby reducing fabrication costs. Second, the wall thickness was picked such that the r/t ratio would have a minimum value of 50 but such that the thickness dimension would be a standard thickness for Lexan sheets. A large value of r/t was desired in order to approach the r/t values of actual aerospace structures. Too large a ratio however would result in a wall whose thickness was inadequate to obtain photoelastic fringe patterns. Hence, 3/32 inch thick sheets were used, as this thickness is adequate for photoelasticity. The final r/t ratio was therefore 54.2. Finally, the length of the cylinder was arbitrarily established as 20 inches, a length that was approximately four times the radius of the cylinder. This length was adequate to allow the investigation of the wave propagation without inter-ference from load nonuniformities that occur near the loaded edge.

Fabrication of the cylinder was accomplished by thermoforming two sheets of Lexan of the appropriate dimensions into half cylinders by the use of a male mold. These two half cylinders were subsequently butt-joined with ethylene dichloride, a solvent of Lexan commonly used as a bonding agent, to form a complete cylinder. As the last step in the cylinder fabrication, both ends of the cylinder were machined with a lathe to obtain the final cylinder length and to assure that both ends were flat and parallel to each other. For ease in identification of location for the photoelastic pictures of the cylinder, lines were scribed on the cylinder circumferentially at one-inch increments and longitudinally at 15-degree increments. A photograph of the final cylinder configuration is shown in Figure 2.

Lexan was used as the material for the cylinder model because Lexan is easily thermoformed into complicated shapes and is a sensitive photoelastic material. In addition, Lexan is an extremely tough material and, as such, survives well in a high-shock environment.

4

EXPERIMENTAL PROCEDURE

Loading Device

For this experimental program, the existing MDAC stress-wave generator was modified to accept a cylinder of the type and dimensions previously described. The stress-wave generator utilizes the discharge of a high-energy, high-voltage capacitor bank to produce a relatively short-duration, high-intensity pressure pulse. This pulse is accomplished by the discharge of the capacitors through a low-resistance, low-inductance return circuit. Portions of this return circuit, called the loading strips, are held in close proximity to each other in such a manner that currents in the strips flow in opposite directions to each other. The resulting magnetic field tends to force the loading strips apart and this force can be quite large if the currents are of sufficient magnitude. A model, butted against one of these load strips, will experience the same load history as the strip and, for a given physical configuration, this load history is a function of the electrical parameters of the system (capacitance, resistance, inductance, and charging voltage). Numerous tests have shown excellent repeatability of the pressure history (on the order of 3 percent). The generator therefore allows the production of repeatable high-pressure, short-duration pulses over flat or curved surfaces. In the past, pressure durations as short as four microseconds have been obtained with maximum pressure magnitudes of 86,000 psi. With the present capacitor system, these values mark the extremes of the performance but generally the device is operated for longer duration pulses of lesser magnitude. For the experiments of this program, the pressure duration was approximately 25 microseconds with a peak magnitude of approximately 2000 psi. This pressure history was achieved by use of two capacitors, each of 12.5 microfarads, charged to 12,000 volts in conjunction with appropriate values of resistance and inductance, empirically determined, for the return circuit. Reference 1 gives a complete description of the stress-wave generator and its principle of operation.

Prior to this test program, all experimentation with the MDAC generator had involved the loading of two-dimensional models only. Hence, the loading strip had been confined to the plane of the model. The loading of a cylinder, however, required the design and fabrication of an entirely different loading fixture. The resulting fixture is shown schematically in Figure 3. As shown in this figure, the current from the transmission line goes around the bottom split cylinder, which serves both as a lower loading strip and inertial block, to the top loading strip, again around a circular path, and finally back to the transmission line. Not shown in this schematic are the 5-mil thick pieces of Mylar used to insulate the loading strips and to insulate the slit in the inertial block. Two other features should be noted in this schematic. First, a cross-section of the top loading strip shows a channel machined in this strip. This channel accepts the Lexan cylinder wall and restrains the loading strip from lateral displacement relative to the cylinder. Second, two sets of Micarta brackets (only one set shown in Figure 3) are attached to the inertial block. These brackets are sized such that the wall of the lexan cylinder will just pass through the brackets and, therefore, prevent the cylinder from undergoing any lateral displacements relative to the lower load strip.

A final part of the loading fixture is called the upper inertial block. This inertial block is simply a 2 inch by 14 inch by 14 inch aluminum plate with a 9 inch diameter hole cut in its center. The placement of this block on top of the Lexan cylinder (a circular groove was cut into the inertial block to accommodate the cylinder wall and was cushioned with a rubber strip) prevents the cylinder from long-time, rigid-body displacement but does not affect the performance of the cylinder relative to the first passage of the stress wave.

Instrumentation

Response of the cylinder to the passage of the stress wave was determined by photoelastic, strain-gage, and accelerometer techniques. The three techniques, as applied to this test program, are described in the following paragraphs.

Static photoelasticity generally involves the fabrication of a two-dimensional model of the part to be analyzed from a photoelastic material. This model is appropriately loaded and observed with a circular polariscope. Basically, a circular polariscope is a device that allows the observation of the birefringence of the model and, for photoelastic materials, this birefringence can be directly related to the state of stress or strain that exists in the model. An observer will see a series of dark and light bands which are collectively called the fringe pattern and the fringe order for a given point is determined by counting the fringes to that point. This fringe order may be related to the difference in principal stresses at that point by the equation

$$\sigma_x - \sigma_y = \frac{nK}{d} \tag{1}$$

where σ_x and σ_y are the principal stresses, n is the fringe order, d is the thickness of the model, and K is a constant of the particular photoelastic material called the stress optical coefficient. At a free edge of a model, one of the principal stresses is zero and the other principal stress, lying tangent to the edge, can be directly determined from Equation 1. This is fortunate because the maximum stresses occur at a surface location for the vast majority of static problems and, therefore, photoelasticity may be used to directly determine these maximum stresses.

The experimental program at hand, however, involved a dynamic condition of stress-wave propagation and, although the validity of Equation 1 still holds, maximum stresses do not necessarily occur at a free boundary. Principal stresses can be determined at free edges, as in the static case, but the resolution of internal stresses can only be accomplished with additional information about the stress field, e.g., the existence of a uniaxial stress field allows such a resolution. For the dynamic case, photoelasticity does produce a dramatic qualitative indication of the stress state.

The photoelastic fringe patterns that result from this wave cannot be directly observed because of their high velocity of propagation (approximately 5000 ft/sec). In the MDAC stress-wave generator, this problem has been overcome by the use of a camera in conjunction with a high-intensity, short-duration light source to photographically stop the movement of the wave. The light source employed uses a spark gap energized by high-voltage capacitors for a half-width-at-half-maximum (HWHM) light duration of approximately 0.5 micro-seconds. The time at which the light source is activated relative to the initiation of the stress wave at the end of the cylinder is controlled by a time-delay circuit. For a given passage of the stress wave, this experimental setup allows the taking of only one photoelastic fringe pattern. Consequently a number of discharges of the stress-wave generator, each with a different light-source delay time, are required to map completely the passage of the stress wave through the model. The validity of this approach rests upon the excellent repeatibility of the load history by the generator plus the operation of the generator at a load level that assures an elastic response of the model. In this manner, the photoelastic manifestation of the interaction of stress waves in models have been recorded in past test programs as well as in the model of this test program.

Modification of the optical path of the polariscope was required for this experimental program to allow the observation of only one wall of the cylinder. The final configuration was as shown in Figure 4. Without the use of the mirrors, the light beam would pass through both sides of the cylinder and the resulting fringe pattern would be a combination of the photoelastic patterns of both sides. Also the mirror scheme allowed the repositioning of the camera and the 6-inch diameter light beam such that the entire length of the cylinder could be sequentially observed, i.e., the limited diameter of the light beam prevented the observation of the entire length of the cylinder in a single optical position.

One biaxial strain gage and seven triaxial strain-gage rosettes were applied to the cylinder model during the course of this test program. In the case of the biaxial gage, one element was oriented in the direction of the cylinder axis and the other in the circumferential direction. Two of the three elements of the triaxial rosettes were also oriented in the axial and circumferential directions, with the third element located between the other elements at an angle of 45 degrees. All elements had active gage lengths of 0.062 inch, a size small enough relative to the wave length to prevent distortion in the gage readout (Reference 2).

A standard wheatstone bridge was employed to read the strain gages in con-junction with a dual-beam Tektronic 555 oscilloscope. The applied excitation voltage was 3.96 volts, a value that resulted in an output of 5 mv for a strain in the active gage of 2500 μ in/in. Calibration of the strain-gage system was by the standard use of shunt resistors. Anamolous apparent strain from heating of the active gage element was minimized by the use of a tempera-ture compensation strain-gage element as a part of the wheatstone bridge. Such a wiring for temperature compensation is commonly used in strain-gage installations.

The discharge of a high-energy capacitor bank produces considerable electro-magnetic noise. This noise will saturate the preamplifiers of the strain-gage electronics in normal strain-gage installations and recovery of the preamplifiers will typically not occur for several milliseconds. Until the recovery of the preamplifier, no data will be recorded. This problem was minimized in these experiments by use of shielded cables in conjunction with a differential oscilloscope preamplifier. Induced noise will still obliterate the oscilloscope trace until the capacitor discharge has completely decayed. This decay occurs at about 40 microseconds after discharge and, hence, limits the closeness to which gages may be read relative to the loaded edge. With a stress-wave propagation velocity in Lexan of 0.063 in/μsec, the closest gage would therefore be at 2-1/2 inches.

The delay trigger feature of the dual beam oscilloscope was employed to delay the sweep of the beam that recorded the strain-gage output. In this manner the sweep was adjusted to occur at the time of the passage of the stress wave over the gage and thus allowed the use of a more sensitive time base.

In the tests of this experimental program, two types of piezoelectric accelerometers were used, the Endevco 2291 and the Endevco 2292. Both accelerometers are designed for the measurement of shock accelerations, both attach to the structure by 1/4-inch diameter holes tapped with 28 threads per inch, and both have masses of 1.3 grams. The 2291 is nominally rated for a peak acceleration of 100,000 g with a resonant frequency of 250 kHz and a sensitivity of 0.00385 picocoulomb/g. The 2292 is designed for a somewhat less severe environment, having a peak acceleration rating of 20,000 g, a resonant frequency of 100 kHz and a sensitivity of 0.130 picocoulomb/g.

Data from both accelerometers were recorded with a dual-beam Tektronic 555 oscilloscope. Two instrumentation schemes were used on both accelerometers. In the first, termed the voltage mode, the accelerometers were connected directly to the oscilloscope preamplifier. This technique is simple but requires an exact knowledge of the capacitance of each component of the accelerometer circuits in order to calibrate the system. This calibration resulted in somewhat non-standard calibration settings in that the voltage outputs from the accelerometers were 0.00734 mv/g and 0.216 mv/g for the 2291 and 2292, respectively. An oscilloscope setting of 0.2 v/cm would therefore correspond to a calibration of 27,200 g/cm for the 2291 and a setting of 10 v/cm would correspond to a calibration of 46,300 g/cm for the 2292.

The second method of accelerometer instrumentation is called the charge mode. A charge amplifier (Umholtz-Dickie Model D-11 was used in these experiments) was inserted in the circuit between the accelerometer and the oscilloscope. The charge mode has the advantage of independence of output upon circuit capacitance plus the ability to calibrate the system such that a unit on the oscilloscope face can be made to correspond to whatever acceleration the experimenter desires. This calibration was typically set at 30,000 g/cm for the experiments of this program.

TEST SEQUENCE AND EXPERIMENTAL RESULTS

The test setup for this program is shown in Figure 5 with the main components of the setup appropriately labeled. Not shown in this figure are the control console for the stress-wave generator and the electronics for the strain-gage and accelerometer instrumentation.

First Test Series

The first test series was conducted on the monocoque cylinder to determine the response of the configuration to an axially propagating stress wave. The results of this test series served as the baseline for subsequent tests and provided insight into the difference in response between that of a cylinder and that of a flat plate, both without inclusions or cutouts.

The initial loadings of the monocoque cylinder were used to obtain photo-elastic data on the cylinder. Photoelastic pictures were taken prior to the installation of strain-gages and accelerometers to provide a basis for deter-mination of the effects that these other two types of instrumentation had on the response of the cylinder. To cover the entire length of the cylinder, the camera and other optical components of the polariscope were placed in three different configurations as previously described in the section on instrumentation. The first optical configuration covered the cylinder from 2 inches from the loaded edge to 8 inches from the loaded edge (hereinafter called the 2-inch location and 8-inch location, respectively). Photoelastic fringe patterns were taken for this optical position at 40 microseconds after initiation of the wave at the loaded edge (hereinafter termed a 40-μsec. delay) and at 10-microseconds intervals thereafter until the delay time equaled 110-μsec. At this delay time the wave was partially out of the field of view and the optics were repositioned to cover the cylinder from the 6-inch location to the 12-inch location. Photoelastic pictures were taken for a 110-μsec delay to a 170-μsec delay, again in 10-μsec intervals. The final optical position covered the cylinder from the 11-inch location to the 17-inch location and photographs were taken at delays of 170-μsec to 250-μsec, again in 10-μsec intervals.

Typical fringe patterns for this test series are shown in Figures 6 and 7 and Figure 6 indicates the manner in which the fringe order is interpreted for these patterns.

After completion of this initial photoelastic mapping, seven strain-gage rosettes were placed on the cylinder at the locations indicated in Figure 1. This figure also indicates the orientation of the triaxial elements of the rosettes relative to the cylinder axis. The initial tests after the installation of the strain-gages were for the determination of the effect that the gages had on the response of the cylinder. This effect was determined by photoelastically observing the cylinder in the area of a gage during the passage of the stress wave. The resulting fringe patterns, Figure 8, when compared to the pattern previously taken for this location, allowed an assess-ment of the strain-gage effect. (It should be noted that the first number of a gage designation, e.g., the designation given in Figure 8, indicates the location of the gage in inches from the loaded edge, the second number indicates the gage's angular location in degrees from the cutout centerline,

9

and the final letter of the designation indicates the orientation of the active gage element, i.e., A stands for axial direction, O for oblique direction (45°), and T for transverse [circumferential] direction.)

Each element of all the rosettes was subsequently read on the oscilloscope to determine the strain history from the passage of the stress wave. In the cases of this first test series, the oscilloscope sensitivity was 2500 μin/in/cm and the sweep rate was 20 μsec/cm. Typical traces are shown in Figures 9 and 10.

In conjunction with the reading of the elements of each gage, a photoelastic fringe pattern was taken for each rosette with the delay time set such that the peak of the wave was located directly beneath the rosette. These data subsequently allowed a comparison between the peak strains, as measured by the strain-gages, and the peak photoelastic fringe orders.

Second Test Series

A rectangular cutout was machined into the cylinder wall to constitute the model configuration of the second test series. Figures 1 and 11 show the location and dimensions and a photograph of the cylinder is shown in Figure 12.

Photoelastic fringe patterns were recorded that covered the five areas shown in Figure 13. As can be seen all of these views were in the region of the cutout. Minimum intervals for fringe pattern time delays were 10 μsec and, for the area covering the cutout, the intervals were 2 μsec. Typical patterns are shown in Figures 14 through 16.

As in the first test series, all strain-gage outputs were recorded with the oscilloscope. For this series, however, a minimum of three oscilloscope records were made for each element, at least one record for each of three sweep rates: 100 μsec/cm, 20 μsec/cm, and 5 μsec/cm. The long-time readings (100 μsec/cm) provided late-time response of the cylinder while the short-time reading (5 μsec/cm) provided greater resolution of the initial pulse. Vertical axis sensitivites were the same as that of the first test series, i.e., 2500 μin/in/cm. Various traces are shown in Figures 17 through 19.

Third Test Series

The third test series was for the determination of the axial acceleration of the cylinder by the use of accelerometers. As previously mentioned, the reason for obtaining accelerometer data was for a comparison of this data for cylinder response with the data obtained by strain-gages and by photoelasticity. Such a comparison would be facilitated if the measurements were made in a uniform field away from the wave disturbance that results from the cutout. For this reason, the accelerometers were mounted on the cylinder in a position diametrically opposite that of the cutout. As the accelerometers are large relative to the wall thickness of the cylinder, it was necessary to design and install a mount for the accelerometers. The mount was also made from Lexan and bonded to the cylinder with ethylene dichloride. Its geometry and location are shown in Figure 20 and the photograph of Figure 21 shows the mount with

the 2292 accelerometer in place. Any decrease in the magnitude of the strain in the mount, relative to the virgin cylinder wall, could be determined by photoelastic observation of the mount.

Acceleration readings were taken using the 2291 and 2292 accelerometers in both the voltage mode and the charge mode. Typical outputs for the voltage mode and charge mode are shown in Figures 22 and 23 respectively. Photoelastic fringe patterns were taken of the propagation of the wave through the mount; Figure 24 shows a typical pattern.

DISCUSSION OF EXPERIMENTAL RESULTS

First Test Series

Examination of the fringe patterns (Figures 6 and 7) taken on the monocoque cylinder before the installation of strain gages shows that the propagating stress wave was uniform in magnitude and velocity of propagation. These patterns show higher fringe orders at the edge of the pattern and, consequently, give the erroneous impression that the cylinder walls in these areas were under a greater state of stress. The light passes through a greater amount of material at the edges of the pattern because of the cylindrical shape of the model. For such a situation an increase in fringe order is expected in that Equation 1 indicates that the observed fringe order, for a given stress state, is directly proportional to the thickness of the material.

Comparison of Figures 6 and 7B shows that 160 μsec are required for the peak of the stress wave to travel 10.1 inches. The velocity of propagation is therefore 0.063 in/μsec. Pulse length in Figure 6 is 1.6 inches, corresponding to a duration of 25 μsec. In Figure 7B however the pulse has dispersed to a length of 1.7 inches for a duration of 27 μsec. These data indicate that although attenuation and dispersion do occur, they are relatively slight over the lengths observed.

Photoelastic fringe patterns (Figure 8) indicate that the strain gages have only a localized effect on the strain field. In Figure 8B, showing the stress wave shortly after passing Gage 9-0, the leading edge of the wave is essentially without distortion, thereby indicating that any disturbing effects from the gages are of a transient nature.

The axial elements of all the rosettes gave peak strains that were approximately 5500 μin/in with durations of about 25 μsec. These values correlate with the duration as determined photoelastically. Also the strain-gage data indicated little or no dispersion as the wave propagated through the cylinder. Comparison of the axial strain data for the 5-inch and 15-inch locations (Figures 9A and 9B) indicate interesting differences in wave shapes. In Figure 9A a decrease occurs in the negative slope of the curve which is not manifested for the corresponding time in the trace of Figure 9B. Furthermore the photoelastic fringe patterns for these locations (Figures 6 and 7B) indicate this same variation in wave shape as a function of position on the cylinder. The cause of this local slope change is not known. The smoothing of such a variation as the wave propagates is, however, predicted by the theory of wave propagation (Reference 3).

The trailing ripple in the strain pulse of Figures 9A and 9B is probably an indication of the underdamped condition of the LRC circuit of the stress-wave generator. Under the conditions of operation of these tests, the current as a function of time in the loading strip is that of an exponentially decaying sine function and each reversal of the current results in the transmittal of a pressure pulse to the model. For the stress-wave generator, theory predicts that the magnitude of any pulse is a function of the square of the current and, consequently, subsequent pulses are of much less magnitude. As the

current as a function of time is a sine function, it also follows that the shape of the pressure pulse should be that of a sine-squared function. For the case at hand only one secondary pulse is detectable in the strain-gage traces. As can be seen from Figures 9A and 9B, this pulse propagates behind the main pulse for the entire length of the cylinder.

The oblique (45°) gages gave peak strain values that were approximately one half of the peak axial strain values while the transverse gages showed that circumferential strain remained at zero throughout the wave passage. The geometry of the model (large r/t ratio) makes the application of plane stress relationships valid. The readings of the oblique and transverse gages indicate that the conditions are more restrictive than plane stress in that the circumferential strain is zero. The stress-strain relationships therefore become

$$\sigma_x = \frac{E \, \epsilon_x}{1-\nu^2} \tag{2}$$

$$\sigma_y = \frac{\nu E \, \epsilon_x}{1-\nu^2} = \nu \, \sigma_x \tag{3}$$

where σ_x and σ_y are the axial and circumferential stresses respectively, E is Young's modulus, ν is Poisson's ratio, and ϵ_x is the axial strain.

The back-to-back triaxial rosettes at the 5-inch, 30-degree location (Figure 1) gave identical readings, within experimental accuracy for all elements. There was therefore no bending in the walls and no radial displacement. This indicates that, for the stress-wave length of these tests, the wall of the cylinder responded in the same manner as a flat plate of the same thickness would have responded. Generally speaking, the geometry of the cylinder would probably not affect the stress-wave response unless the length of the wave were equal to, or greater than, the circumference of the cylinder.

Generally, shock responses of aerospace vehicles are described in terms of acceleration as a function of time for various points on the vehicle or in terms of a shock spectra consisting of response representations obtained by reduction of acceleration histories. In order for model data to be readily used by the aerospace industry, it is necessary that the raw model data be reduced to acceleration histories or reduced to shock spectra. The last test series of this experimental program determined accelerations directly by accelerometers. The disadvantage of such an approach for model application is that the available accelerometers are large relatively to the structure of the model. One then has the classic case of altering the response one wishes to measure by the very act of making that measurement. For this study photo-elasticity and strain-gage techniques were investigated for the feasibility of reducing these types of data to accelerations of the model. The following paragraphs describe how this was accomplished.

For a plane wave traveling in the direction of increasing x, displacement as a function of position and time may be written as

$$u = f(c_0 t - x) \tag{4}$$

where u is displacement, f represents the function, c_0 is the propagation velocity, and t is time. Separate differentiating of Equation 4, first with with respect to x and then with respect to t, will yield

$$\frac{\partial u}{\partial x} = - f'(c_0 t - x) \tag{5}$$

$$\frac{\partial u}{\partial t} = c_0 f'(c_0 t - x) \tag{6}$$

Solving both equations for $f'(c_0 t - x)$ and equating the results gives

$$\frac{\partial u}{\partial t} = - c_0 \frac{\partial u}{\partial x} \tag{7}$$

As $\partial u/\partial t$ is the particle velocity (v_x) and $\partial u/\partial x$ is the strain in the x direction (ε_x) Equation 7 becomes

$$v_x = - c_0 \varepsilon_x \tag{8}$$

Differentiation of Equation 8 with respect to time will yield the acceleration

$$A_x = - c_0 \frac{\partial \varepsilon_x}{\partial t} \tag{9}$$

where A_x is acceleration. Equation 9 simply states that the acceleration is equal to the propagation velocity times the instantaneous slope of the strain history for any given time. It should be realized that the foregoing argument

14

is valid only for the case of the propagation of a plane stress wave. In practice Equation 9 means that a strain history may be reduced to an acceleration history by a point-by-point measurement of the slope of the strain history. The disadvantage of this approach is that small variations in the strain history may result in large variations in the slopes. For the present study, however, the strain histories are smooth curves and such a reduction as herein described is both straightforward and accurate.

Maximum acceleration is then determined by measurement of the maximum slope. For example, Figure 18B shows the strain history of Gage 9-0-A. The maximum strain rate is calculated as -754 in/in/sec. This value, along with the velocity of propagation of 0.063 in/μsec, results in a maximum acceleration of 126,000 g.

In like manner the slope of the strain may be obtained from the photoelastic data. This is accomplished by determining the fringe order at a given point as a function of time. Such a determination requires a series of photographs of the fringe patterns at the point, each taken at slightly different times. The data obtained from these photographs would be a series of discrete points plotted as a function of time and connection of the points would yield a continuous curve of fringe order versus time. Application of Equation 1, for conversion of fringe order to difference in principal stress, and Equations 2 and 3, for conversion of difference in principal stress to strain, results in a plot of strain versus time. The procedure for obtaining acceleration from this stage onward is then identical to that employed with the strain-gage data.

There are certain difficulties in the reduction of photoelastic data to obtain accelerations. First, a large number of photographs are required to accurately record the changing photoelastic pattern and the minimum time separation between these photographs would be a function of the maximum strain rate. Typical required separation times are on the order of two microseconds between photographs. For a stress wave typical of this test series (duration of 25 μsec), such a time separation would require a minimum of 12 photographs. Second, determination of exact fringe order in most cases would require extra-polation to non-integral values of fringe orders. These non-integral values must be estimated from the photographs and such estimation could give rise to inaccuracies. Finally the reduction of differences in principal stress to axial strain requires additional information as to the type of stress field that exists at the point of interest. In the monocoque configuration, for instance, it is known that the conditions are that of plane stress with zero circumferential strain. Without such additional information the photoelastic data cannot be reduced to accelerations. A method of surmounting this limitation is possible, however, and is discussed in the section on conclusions and recommendations. Accelerations determined from strain gages were used in the data reduction for the test series of this program, rather than those determined from photoelastic data, because of the relative ease with which strain-gage data may be reduced to accelerations.

The assumption that the pressure applied to the loaded edge is a sine-squared function of time gives an interesting check on the validity of the maximum acceleration measured with strain gages. Again assuming classical wave propagation theory, it can be shown that the maximum acceleration for a strain pulse having a sine-squared shape is

$$A_{max} = - \frac{c_o \, \epsilon_M \, \pi}{P} \qquad (10)$$

where c_o is as previously defined, ϵ_M is the maximum strain (-5500 μin/in) and P is the strain duration time (25 μsec). Substitution of these values will result in a maximum acceleration of 115,000 g, a value very close to the measured value.

Second Test Series

As was expected the photoelastic fringe patterns taken prior to the arrival of the stress wave at the cutout are identical to those patterns taken on the uncut cylinder. The interaction of the stress wave with the cutout are shown in Figures 14 through 16. Three phenomena are readily apparent in these figures. First, the reflection of the compression wave at the lower edge of the cutout results in the propagation of a tension wave in the opposite direction from the initial compression wave. Second, the interaction of the stress wave with the cutout results in a stress concentration at the corners of the cutout. This is manifested in the large increase in fringe order that occurs at these corners. Figure 14B indicates that the maximum fringe order at these corners is 10, compared to a maximum fringe order of 4-1/2 at a location away from the cutout. These fringe orders, together with the assumption that a plane-stress, uniaxial-strain field exists in the cylinder wall and that a plane stress field exists at the edge of the corner, results in a strain concentration value of 1.62 and a stress concentration is 1.40. For this program strain and stress concentrations are defined as the maximum values of such quantities at the location in question, e.g., the edge of the cutout, divided by the maximum values of such quantities in the free field of the cylinder.

Finally, the photographs indicate the formation of oblique relief waves, (shown in Figure 15A) on both lateral edges of the cutout, that propagate into the remainder of the cylinder at an angle of approximately 45 degrees. As previously mentioned the strain field of the stress wave, prior to the arrival at the cutout, has no strain component in the circumferential direction and, hence, there exists a biaxial stress field. For a free edge, however, there can exist no stress component perpendicular to this free edge, and when the stress wave arrives at the cutout, the circumferential component of the biaxial stress field is relieved at the edge of the cutout. This relief propagates into the remainder of the cylinder and gives rise to the oblique relief waves.

Figure 15B shows the bending of the stress wave around the back of the cutout. The subsequent reunification of the wave components (Figure 16) results in a fringe order considerably reduced from the free-field fringe order. As can be seen in Figure 16B this reduction is by a factor of approximately two when the peak of the wave has propagated a distance away from the cutout equal to the height of the cutout.

The strain-gage traces for the second test series (Figures 17 through 19) further illustrate the phenomena observed in the photoelastic patterns. Figure 18A, showing the output of Gage 9-0-A, dramatically demonstrates the passage of the initial compression wave and the subsequent passage of the tension wave that reflects from the lower edge of the cutout. This phenomenum of wave propagation and reflection is also shown in Figure 17B, the trace of Gage 15-0-A taken at a sweep rate of 100 μsec/cm. Point A of this trace is the initial passage of the wave (note that the magnitude of this passage is approximately half that of the free field shown in Figure 17A, thereby correlating with the photoelastic results), Point B is the tension reflection of the wave from the free end of the cylinder and Point C is the compression reflection of this tension wave from the top edge of the cutout. In all cases the arrival times of the waves correlate with the measured propagation velocity of 0.063 μin/sec.

Third Test Series

As mentioned previously, two types of accelerometers were each employed in two different types of data acquisition modes to measure the acceleration of the cylinder wall. The acceleration histories, shown in Figures 22 and 23, indicate that in all cases the measured acceleration was approximately 62,000 g. This value is considerably less than the acceleration of 126,000 g determined by the reduction of the strain histories obtained from the strain-gages. The mount to which the accelerometers were attached had a depth of 0.375 inch compared to the underlying wall thickness of 0.097 inch. With this large difference in thickness, a reduction in acceleration is not surprising. The task then became that of correlating the acceleration measured on the mount with that calculated from the strain-gage outputs. Two approaches were taken to resolve this issue.

First, photoelastic pictures were taken of the stress wave as it propagated into, through, and beyond the accelerometer mount. One such picture is shown in Figure 24 and, as can be seen, resulted in considerable disturbance to the free-field photoelastic pattern. This pattern also allows an assessment of the average strain in the mount and cylinder wall directly under the mount relative to the strain in the cylinder wall in a region undisturbed by the mount. Such an assessment is accomplished by comparison of the maximum fringe orders in each position in conjunction with certain assumptions concerning the stress-strain field in these two regions. The stress-strain relationship for the cylinder are given in Equations 2 and 3. These two equations may be combined to give the following expression for the axial strain

$$\varepsilon_x = (\frac{1+\nu}{E}) \, (\sigma_x - \sigma_y) \tag{11}$$

Because the length of the wave is long compared to the cross-section dimensions of the mount, a condition of uniaxial stress is assumed to exist in the mount. The applicable stress-strain relationships are therefore

$$\sigma_x = E \, \epsilon_x \tag{12}$$

$$\sigma_y = 0 \tag{13}$$

For later convenience Equations 12 and 13 are rewritten as

$$\epsilon_x = \frac{1}{E} (\sigma_x - \sigma_y) \tag{14}$$

The division of Equation 14 by Equation 11 will result in an expression for the ratio of the axial strains. This expression reduces to

$$\frac{(\epsilon_x)_1}{(\epsilon_x)_2} = \left(\frac{1}{1+\nu}\right) \frac{(\sigma_x - \sigma_y)_1}{(\sigma_x - \sigma_y)_2} \tag{15}$$

where the subscripts 1 and 2 refer to the mount and cylinder respectively. These differences in principal stress are determined by the photoelastic fringe patterns as applied to Equation 1. The ratio of the differences in principal stresses may be written

$$\frac{(\sigma_x - \sigma_y)_1}{(\sigma_x - \sigma_y)_2} = \frac{n_1 \, d_2}{n_2 \, d_1} \tag{16}$$

where n is the maximum fringe order (17 fringes and 4-1/2 fringes for the mount and cylinder wall respectively) and d is the optical thickness (0.472 inch for the combined thickness of the mount and cylinder wall and 0.097 inch for the cylinder wall alone). The application of these values plus the value for Poisson's ratio of 0.37 to Equation 15 and 16 results in a ratio for the axial strains of 0.56. The strain in the mount is therefore 56 percent of the strain in the cylinder wall. This result can be applied to determine the ratio of the

maximum accelerations if it is assumed that the axial strain histories of the mount and cylinder wall are of the same shape, differing only in magnitude. If such a condition exists, then the ratio of the maximum accelerations equals the ratio of the maximum strains. The maximum accelerations in the mount should therefore be 56 percent of the maximum acceleration of the cylinder wall. Assuming that the wall acceleration is 126,000 g (as determined by strain-gages) then the acceleration in the mount would be 71,000 g. Considering the assumptions made in the foregoing analysis, this value is reasonably close to the accelerometer value of 62,000 g; this difference amounting to 14 percent.

As a second approach to the determination of the validity of the accelerometer readings, a biaxial strain-gage was placed on the accelerometer mount in the position shown in Figure 20. The output of this gage is shown in Figure 25 and indicates the existence of a biaxial strain field and hence the possibility of a uniaxial stress field.

The reduction of the axial strain history gives a maximum strain rate of -357 in/in/sec corresponding to a maximum acceleration (Equation 9) of 59,000 g, a value approximately 4 percent below that obtained with the accelerometers.

A summary of the values obtained by the three instrumentation techniques for accelerations is given in Table 1.

A comparison of the accelerometer trace of Figure 23A for the 2291 with that of Figure 23B for the 2292 shows that the positive portions of the traces are nearly identical. The negative portions are different, however, in that local oscillations occur in this portion in the trace from the 2292 accelerometer but do not appear in the trace from the 2291 accelerometer. Figure 23B shows that five cycles of local oscillation occur for the 2292 in 36 microseconds, corresponding to a frequency of 139 kHz. This frequency is close to the manufacturer's stated resonant frequency of 100 kHz for this transducer and these local oscillations are probably the excitation of this resonance. No such oscillations appear in the traces for the 2291 at a frequency of 139 kHz nor are there oscillations at 250 kHz, the resonant frequency of the 2291 accelerometer.

The peak magnitudes of the negative portions of the acceleration histories are less than that of the positive portions. This decrease in the absolute value of the maxima is reflected in both the strain-gage data and the photoelastic data. Figure 17A, showing the axial trace of Gage 5-0, indicates that the absolute value of the slope of the trailing portion of the strain wave is of lesser magnitude than the leading portion. This then translates into a lesser value for peak accelerations at the trailing portion of the wave. This nonsymmetry is also manifested in many of the photoelastic fringe patterns, e.g., Figure 6, where the increased spacing in the trailing portion of the wave are interpreted as a decrease in the maximum strain rate.

For a further characterization of the shock pulse, the outputs obtained in the charge mode of both accelerometers (Figure 23) were reduced to produce shock spectra. This was accomplished by first making photographic transparencies of the oscilloscope photographs and using these transparencies to reduce the

accelerometer traces to digital data by the MDAC Graphicon System. The Graphicon consists of a light table in conjunction with a light pen. The tracing of the oscilloscope record with the light pen produces a digitized record of the acceleration that is stored on magnetic tape. In the system used, this digitization results in 1024 data points. The magnetic tape was processed on an XDS-930 computer with the MDAC ELS-1 computer program to produce the shock spectra. Also outputted by this program is a plot of the digitized acceleration history. The acceleration histories and shock spectra are shown in Figures 26 through 29 for both accelerometers.

As would be expected, the shock spectra are very similar for the 2291 and 2292. The peak of both occur at about 150,000 g. This value is about 2-1/2 that of the peak acceleration of the acceleration histories and such a ratio is characteristic of shock spectra. It is interesting to note the local peak in the negative response portion of the shock spectra of the 2292 in the region of 100,000 kHz. This local peak is apparently from the resonance excitation, and as such does not appear in the spectrum of the 2291.

SIMILITUDE FEASIBILITY STUDY

Introduction

The feasibility of scaling model data to determine the dynamic response of full-size prototypes depends fundamentally on what physical parameters are important in the response problem. At one end of the spectrum are linear elastic response problems for homogeneous, one-dimensional structures that are insensitive to strain rate and that are undamped. At the other end are response problems for structures whose material consitutive relationships are of such complexity as to make scale modeling extremely difficult if not impossible. The present study is concerned with metallic structures of isotropic materials and scale models of plastic materials. It is helpful to first review the modeling requirements of three-dimensional elasticity for an isotropic body. Next the feasibility of scale modeling when stress depends on strain rate as well as strain will be investigated and, finally, model fabrication problems will be reviewed.

Model Requirements for an Isotropic Body

Consider an isotropic, homogeneous, linear elastic body that occupies a volume V bounded by a surface B as shown in Figure 30. The undeformed body is initially at rest in a uniform gravitational field $g \underset{\sim}{d}$. The body is subjected to body forces $\underset{\sim}{f}$ ($\underset{\sim}{Z}$, t) in the interior, surface tractions $\underset{\sim}{S}$ ($\underset{\sim}{Z}$, t) on a portion of the bounding surface, B_S, and the displacement vector $\underset{\sim}{u}$ ($\underset{\sim}{Z}$, t) is prescribed zero on the remaining portion of the bounding surface, B_u. The coordinates z_i of a point $\underset{\sim}{Z}$ are with respect to an orthonormal Cartesian frame that can be considered an inertial frame. The field equations for infinitesimal displacements are

$$\frac{\partial \sigma_{ij}}{\partial z_j} + f_i = \rho \frac{\partial^2 u_i}{\partial t^2} + \rho g d_i \tag{17}$$

$$\sigma_{ij} = 2\mu\varepsilon_{ij} + \lambda \delta_{ij} \varepsilon_{kk} \tag{18}$$

$$\varepsilon_{ij} = 1/2 \left(\frac{\partial u_i}{\partial z_j} + \frac{\partial u_j}{\partial z_i}\right) \tag{19}$$

where σ_{ij} and ε_{ij} are respectively the components of the stress and strain tensors of classical elasticity; u_i are the components of the displacement

vector; d_i are the direction cosines of the gravitational field; λ and μ are the Lame constants of the material, and ρ is the mass density. The initial conditions are

$$u_i\ (\underset{\sim}{Z},\ 0) = 0 \tag{20}$$

$$\frac{\partial}{\partial t}\ u_i\ (\underset{\sim}{Z},\ 0) = 0 \tag{21}$$

and the boundary conditions are

$$\sigma_{ij}\ n_j = S_i\ (\underset{\sim}{Z},\ t);\ \underset{\sim}{Z} \in B_s \tag{22}$$

$$u_i\ (\underset{\sim}{Z},\ t) = 0;\ \underset{\sim}{Z} \in B_u \tag{23}$$

where n_j are components of the outward unit normal $\underset{\sim}{n}$ to B_s at the point $\underset{\sim}{Z}$ on this surface. These conditions and the field equations completely determine the response $\underset{\sim}{u}\ (\underset{\sim}{Z},\ t)$, $\sigma_{ij}\ (\underset{\sim}{Z},\ t)$ and $\varepsilon_{ij}\ (\underset{\sim}{Z},\ t)$ and hence identify all the physical parameters important in the response problem. In general it is not necessary to know the governing equations to identify the important physical parameters in the response problem. In fact, having identified the important physical parameters, the modeling requirements can be determined using the Buckingham Pi theorem without recourse to the governing equations. Counting the components of a vector or tensor as only one parameter, there are eleven physical parameters that determine the response which implies there are eight dimensionless Pi terms that are sufficient to describe the response. The eleven parameters* are σ_{ij}, f_i, g, u_i, t, S_i, λ, μ, ρ, ℓ, and z_i, and a convenient set of Pi terms is

$$G\ (\frac{\sigma_{ij}}{\mu},\ \frac{f_i\ell}{\mu},\ \frac{\rho g\ell}{\mu},\ \frac{z_i}{\ell},\ \frac{u_i}{\ell},\ \frac{t}{\ell}\ \sqrt{\frac{\mu}{\rho}},\ \frac{\lambda}{\mu},\ \frac{S_i}{\mu}) = 0 \tag{24}$$

The quantity ℓ is any convenient characteristic length.

---

* Strain ε_{ij} and the direction cosines d_i are already dimensionless.

These are not unique but are a commonly used set of dimensionless parameters. Equation 24 can also be written

$$\frac{\sigma_{ij}}{\mu} = F \left(\frac{f_i \ell}{\mu}, \frac{\rho g \ell}{\mu}, \frac{z_i}{\ell}, \frac{u_i}{\ell}, \frac{t}{\ell}\sqrt{\frac{\mu}{\rho}}, \frac{\lambda}{\mu}, \frac{S_i}{\mu} \right) \qquad (25)$$

The scaling laws that are implied by Equation 25 can be stated as

$$\left. \begin{aligned}
\left(\frac{\sigma_{ij}}{\mu}\right)_m &= \left(\frac{\sigma_{ij}}{\mu}\right)_p \\[2mm]
\left(\frac{f_i \ell}{\mu}\right)_m &= \left(\frac{f_i \ell}{\mu}\right)_p \\[2mm]
\left(\frac{\rho g \ell}{\mu}\right)_m &= \left(\frac{\rho g \ell}{\mu}\right)_p \\[2mm]
\left(\frac{z_i}{\ell}\right)_m &= \left(\frac{z_i}{\ell}\right)_p \\[2mm]
\left(\frac{u_i}{\ell}\right)_m &= \left(\frac{u_i}{\ell}\right)_p \\[2mm]
\left(\frac{t}{\ell}\sqrt{\frac{\mu}{\rho}}\right)_m &= \left(\frac{t}{\ell}\sqrt{\frac{\mu}{\rho}}\right)_p \\[2mm]
\left(\frac{\lambda}{\mu}\right)_m &= \left(\frac{\lambda}{\mu}\right)_p \\[2mm]
\left(\frac{S_i}{\mu}\right)_m &= \left(\frac{S_i}{\mu}\right)_p
\end{aligned} \right\} \qquad (26)$$

Where the subscript m denotes model and p denotes prototype. The strains ε_{ij} and direction cosines d_i must also be equal. It should be emphasized that the relations of Equation 26 are not dependent on the governing equations;

they depend only on the Buckingham Pi theorem. The strain-displacement
equations and stress-strain equations can be nonlinear for example. The
interpretation of the relationships given in Equation 26 is relatively
straightforward. For instance, the first relationship of Equation 26 means
that stresses in the prototype can be determined simply by multiplying the
stresses measured in the model by the ratio μ_p/μ_m, provided that all the
other conditions of Equation 26 are satisfied. The satisfaction of Equation
26 can, however, require stringent model design, especially if gravity forces
are important. When the model and prototype are of the same material,
simulation of these forces requires either a full-scale model or requires the
changing, somehow, of the magnitude of these force fields. The problem could
be further compounded if the model and prototype were made of different
material. Even when gravity forces are unimportant, Equation 26 requires
replica modeling and requires the use of materials that have the same Poisson's
ratio, i.e., $(\lambda/\mu) = 2\nu/(1-2\nu)$.

The use of models that have Poisson's ratios different from the prototype
require an examination of the influence of Poisson's ratio on response. Past
experience in photoelasticity for static loadings of models have shown that
differences in Poisson's ratios generally have insignificant effects in the
prediction of stresses in the prototype (References 4, 5, and 6). As the
similitude relationships for the static case are the same as those of the
dynamic case (Equation 26), with the exception that the relationship
$(t/\ell \sqrt{\mu/\rho})_m = (t/\ell \sqrt{\mu/\rho})_p$ need not be satisfied, it is possible that the effect
of different Poisson's ratios may also be insignificant for the dynamic case.
An indication of the effect for the dynamic case can be obtained by an
examination of the equations of motion (Navier's Equations). First a change
of variables will be made to non-dimensionalize the equations per Equation 26.

$$\xi_i = z_i/\ell, \quad u_i^* = u_i/\ell$$

$$\tau = (t/\ell)\,\sqrt{\mu/\rho}, \quad f_i^* = f_i\,\ell/\mu, \quad g^* = \rho g\,\ell/\mu$$

and the dilatation, $e \equiv \varepsilon_{kk}$, defined so that the equation can be written

$$\left(\frac{1}{1-2\nu}\right) \frac{\partial}{\partial \xi_i}\,(e) + \nabla^2 u_i^* + f_i^* = g^* d_i + \frac{\partial^2}{\partial \tau^2}\,(u_i^*) \tag{27}$$

The only term explicitly dependent on Poisson's ratio is the dilatation term
(i.e., hydrostatic stress term). The value of ν for Lexan is near 0.37 while
ν for aluminum is near 0.30 and, in this range, the coefficient $1/(1-2\nu)$ does

change significantly. To determine if this distortion will in turn produce a significant effect on dynamic response, MDAC has a two-dimensional computer simulation code (TOODY) that can be used to predict response for a reference shape using different values of Poisson's ratio. Should the response change significantly, a prediction factor to correct this distortion could possibly be determined empirically for the actual structural shape. This would require the testing of several plastic models with different values of ν_m and plotting,

for example, the strain (or any of the nondimensional parameters of Equation 26) versus ν_m. The ratio of the nondimensional strain at the correct ν and the distorted ν would be interpolated from this graph and used directly to predict prototype response. Although the determination of a prediction factor is a standard engineering procedure (Reference 7), the need to fabricate and test several models, plus the difficulty or impossibility of adequate variation of Poisson's ratio in these models, make the application of this procedure questionable for the type of tests described in this report. In any event should the effects of difference in Poisson's ratios prove unacceptable, there still remains to the experimenter the use of models made from the same materials as the prototype.

Strain-Rate Effects

In the present study the loading conditions are impulsive in nature and the physical parameters affecting structural response must be re-examined. This will be done using the simple Voigt viscoelastic model and a more general viscoelastic model (Reference 8) that satisfies fundamental thermodynamic considerations. The Voigt model traditionally has been applied to describe viscoelastic behavior because of its relative simplicity. However, as shown in Reference 8, the Voigt model exhibits implausible thermodynamic behavior. This is unimportant at low strain rates but, for high strain rates, use of the Voigt model is questionable. The more general viscoelastic model has no such inherent limitations and consequently is valid at high as well as low strain rates. In an effort to be comprehensive both models are considered and it will be shown that the scale modeling requirements for the more general model are quite different from those obtained for the Voigt model.

Consider first the one-dimensional Voigt relation for stress as a function of strain and strain rate.

$$\sigma = E \epsilon + \eta \dot{\epsilon} \tag{28}$$

This identifies one new physical parameter, η, that must be considered to determine the structural response. The units of this parameter are $FL^{-2} T$ and using the Buckingham Pi theorem again we obtain the additional modeling requirement

$$\left(\frac{\eta}{\ell\sqrt{\mu\rho}}\right)_m = \left(\frac{\eta}{\ell\sqrt{\mu\rho}}\right)_p \tag{29}$$

This requirement is similar to that obtained for body forces and gravitational forces in that the rate constant η must be changed in proportion to ℓ. The only manner in which this could be satisfied would be to determine the parameters of η, μ, and ρ for both the prototype and model materials, apply these values to Equation 29, solve for the ratio ℓ_m/ℓ_p, and apply this ratio to the scaling of the model relative to the prototype. It is unlikely that the ratio would be of a suitable value. Furthermore, if the prototype and model are of the same material, the ratio is one and the model would be identical to the prototype. In fact a small model of the same material will accentuate strain-rate effects according to the Voigt model since

$$\left(\frac{\eta}{\ell}\right)_m > \left(\frac{\eta}{\ell}\right)_p \tag{30}$$

These differences will be small if the condition $E\,\varepsilon_{max} \gg \eta\,\dot{\varepsilon}_{max}$ holds. Reference 9 indicates this is true of metals and plastics at structural-response strain rates ($\dot{\varepsilon} \sim 10^3$ in/in/sec) but that it is not true of plastics at shock-response rates ($\dot{\varepsilon} \sim 10^6$ in/in/sec). The strain rates associated with the Lexan models of the present study were all under 10^3 in/in/sec. If higher strain rates are necessary, empirical correction curves obtained with different model materials offer one possible solution. This assumes of course that the materials are all governed by the Voigt model.

The validity of a Voigt model is questionable at very high strain rates for most engineering materials in that these materials possess an initially elastic response not predicted by a Voigt model. Valanis, Reference 8, page 349, demonstrates that "contrary to expectation the rate of irreversible entropy production increases with the square of the rate of strain according to [the Voigt] theory." The effect of strain rate will now be reconsidered on the basis of a model exhibiting behavior that is thermodynamically plausible. This model is based on a viscoelastic potential that includes thermodynamic coordinates and leads to the stress response at a point as

$$\sigma_{ij}(t) = C_{ijk\ell}\varepsilon_{k\ell}(t) + \int_{-\infty}^{t} C^1_{ijk\ell}(t-\alpha)\,\frac{\partial\,\varepsilon_{k\ell}}{\partial\alpha}\,d\alpha \tag{31}$$

26

which for isotropic materials is

$$\sigma_{ij}(t) = \lambda \epsilon_{kk}(t)\delta_{ij} + 2\mu\,\epsilon_{ij}(t) +$$

(32)

$$\delta_{ij}\int_{-\infty}^{t}\lambda^1(t-\alpha)\frac{\partial\epsilon_{kk}}{\partial\alpha}\,d\alpha + 2\int_{-\infty}^{t}\mu^1(t-\alpha)\frac{\partial\epsilon_{ij}}{\partial\alpha}\,d\alpha$$

This identifies two new physical parameters $\lambda^1(t)$ and $\mu^1(t)$, both functions of the history of deformation, that must be considered to determine structural response. The units of these parameters are FL^{-2} and using the Buckingham Pi theorem we obtain

$$\left[\frac{\lambda^1(t_m)}{\mu}\right]_m = \left[\frac{\lambda^1(t_p)}{\mu}\right]_p$$

$$\left[\frac{\mu^1(t_m)}{\mu}\right]_m = \left[\frac{\mu^1(t_p)}{\mu}\right]_p$$

(33)

where model time and prototype time are related as in Equation 26. These requirements indicate that if the model and prototype are of the same material, the nondimensional response will be the same provided the nondimensional deformation history in model time is the same as the nondimensional deformation history in prototype time. Equation 33, in conjunction with Equation 26, therefore indicate the feasibility of accurately determining prototype strain-rate effects from measured strain-rate effects in a model.

Fabrication Effects

In the previous discussion the possibility of replica scale modeling of all important dimensions was tacitly assumed. In actuality the fabrication of a true geometrical model could be difficult in that some portions of the prototype often are relatively small compared to the overall dimensions of the prototype. The construction of a model of reasonable overall size would then require that these portions be extremely small. A serious manisfestation of this problem occurs in the case of models of vehicles that have very large r/t values. For example, a vehicle with an r/t of 500 would require a wall thickness of 0.010 inch in a 10 inch diameter model, in contrast to the 0.097 inch wall thickness of the model of the test program described in this report. The wall thicknesses required on such models may be too small for an accurate geometrical reproduction. One possible solution to such a situation, is to construct a distorted model, distorted in the sense that the thickness

dimensions of the model violates a true geometrical scaling. The major difficulty of using a model distorted in the thickness dimension occurs when the response of the model to bending forces and to in-plane forces are both of importance. In such cases the ratio of the dynamic response of the distorted model to the dynamic response of the prototype will be a continually varying quantity. Hence there will be no set multiplier to convert model response to prototype response.

The use of distorted models in static testing is not an uncommon practice (Reference 7) and has previously been outlined in this report concerning the violation of the Buckingham Pi relationship (Equation 26) involving Poisson's ratio. In all probability, however, the dynamic aspects of a dimensionally distorted model will not in general be compensatable.

Consequently it appears that it will be necessary to adhere to strict geometrical models. The consequence to the experimenter of strict adherence to true geometrical models may not be as serious as it first appears. Although the diameter of the model used in this test program was just over 10 inches, there is nothing inherent in the technique which prohibits the use of larger models. A diameter of 20 inches, for instance, would result in a wall thickness of 0.020 inch for an r/t of 500 and a wall thickness of 0.010 inch for an r/t of 1000. Fabrication of model cylinders of either of these thicknesses are within the present state-of-the-art.

There are other problems involved in true geometrical modeling that, although not as important as a violation of the r/t ratio, must nevertheless be considered. Actual flight hardware often has irregular construction detail that may make it impossible to achieve truely replica modeling. This is particularly true of joints and fasteners but it could also include such things as residual stresses caused by fabrication. Consider for example a welded part that has very thin gages when scaled. If the scale model is also welded, the resulting joint may have vastly different properties because of thermodynamic differences in the two welding processes. If a substitute mechanical joint or no joint at all is used, the vibration characteristics of the model and prototype may differ considerably. Perhaps the most noteworthy example of the problems that can arise from joint and fastener differences is the 1/10 scale replica model of the Apollo/Saturn V, described in Reference 10. This was a quality model in which serious efforts were made to replica model practically the entire structure. In spite of this there were obvious differences in bolted flange joints because, as Reference 11 describes it, "the thin-flange ring frames used in the scale model would not hold their planar shape." In addition to these differences, the gravity forces on the structure could not be scaled and this allowed some joints to open during vibration testing.

Another fabrication difference that can be important in scale model construction is caused by tolerances. In most instances these differences are unimportant but, if the response is sensitive to imperfections, then these differences can be significant. Buckling of thin walled shells is an example of a structural response sensitive to imperfections.

CONCLUSIONS AND RECOMMENDATIONS

Conclusions

The foregoing experimental and analytical conclusions lead to the one central conclusion that the determination of the response of prototype aerospace structures to pyrotechnic shock loads by the use of laboratory models is feasible, subject only to the usual limitations encountered in all model testing. The potential cost reduction for the characterization of shock response makes such a method highly desirable.

The tests of this program showed that photoelastic cylindrical models may be successfully fabricated and loaded with short duration, uniform loads in the MDAC stress-wave generator. Both photoelastic and strain-gage techniques can be used to determine the response of such models to the resulting stress wave as this wave propagates through the model. The photoelastic data give quantitative information on stress and strain concentrations at free edges of the model and qualitative information in the remaining areas of the model. Strain histories from the strain-gage data can be readily reduced to accurate acceleration histories. Accelerometers may also be used to get accelerations that occur in the model and the accelerations indicated the excellent accuracy with which accelerations may be obtained by reduction of the strain-gage data. It should be noted that, for this test program, the accelerometers were not directly attached to the model but rather were held by a mounting block to the model. Consequently comparisons of accelerations determined by accelerometers to accelerations determined by other types of instrumentation required appropriate compensation factors to account for the effects of the accelerometer mount. The experimental portion of this program also showed that shock spectra for the model response may be obtained by reduction of the acceleration histories.

The modeling requirements for general isotropic structures given by Equation 26 indicates the feasibility of model testing for dynamic response if body forces and gravitational forces can be neglected. The use of substitute isotropic materials with different Poisson's ratios may cause response differences. In this event it will probably be necessary to restrict model materials to the same materials as used in the prototype, although there does exist the possibility of determining empirical correction curves based on tests with different plastic materials. Strain rate modeling requirements for two viscoelastic theories were also given. The requirements from the thermo-dynamically plausible theory indicate that scale model tests that accurately model strain rate effects are feasible. Moreover, other investigations (Reference 9) indicate the effect of strain rates under 10^3 in/in/sec are unimportant for impulsively loaded metallic and plastic structures. Since the strain rates associated with structural response are less than this it appears feasible to obtain full-scale response data for impulsively loaded structures from Lexan models. The response may include geometric nonlinearities but stress levels must be kept in the linear elastic range. This requirement stems from differences in the strain hardening characteristics of Lexan and most metals.

The most efficient use of plastic scale models is in design trade studies where a number of concepts can be evaluated using inexpensive models. The feasibility of such testing was established provided (a) that body forces can be neglected and (b) that response differences that result from differences in Poisson's ratio between the prototype and model materials are insignificant or that correction factors can be obtained to compensate for these differences. The feasibility of prototype prediction by model testing was also established subject to certain fabrication limitations. As a practical matter, structures with complex joints and fasteners or imperfection sensitivities will be difficult to simulate in a scale model. An awareness of this situation is important but it does not limit the basic capability of scale model testing. Furthermore, it will be necessary to construct relatively large models in order to conform to strict geometrical scaling in the case of models that model vehicles having large r/t ratios.

It is well to note that the unresolved problems associated with dynamic model testing, which are discussed in this report (body forces, Poisson's ratio, and exact scaling), are not unique to dynamic modeling but rather are general problems associated with all model testing.

Recommendations

In the present technique the photoelastic fringe patterns can be reduced to quantitative data only at the location of free edges or at locations where other, specialized information is available about the stress or strain field. At all other locations the photoelastic patterns can only give a qualitative indication of the stress-wave behavior. The expansion of the polariscope system to include laser interferometry would allow the resolution of stress components at any location. In this technique laser isopachic fringe patterns, which are proportional to the sum of the principal stresses, are combined with conventional photoelastic patterns, which are proportional to the difference of the principal stresses, to obtain the principal stresses. This combination is particularly beneficial to dynamic problems in that maximum stresses do not generally occur at edge locations.

In the similitude study of this program, conclusions were made as to the relationships that must be satisfied to relate model response to prototype response. The fabrication and testing of an aluminum model would allow an assessment of the validity of these similitude relationships if this model was subjected to the same test program as the Lexan model described in this report. Furthermore, the fabrication and testing of models made from materials of different Poisson's ratios would allow an assessment of the effect of not satisfying the similitude relationship that requires identical Poisson's ratios for the materials of the model and prototype. Variation in the Poisson's ratio for such models could possibly be accomplished by the use of epoxy resins mixed in suitable ratios. In conjunction with an experimental program, an analysis should be conducted to determine the effect of this violation of Poisson's ratios, by use of the TOODY two-dimensional computer code.

The modeling of an actual vehicle and the testing of this model would allow the ultimate in the investigation of the feasibility of this modeling technique. For such a program there must of course exist extensive data on the response of the modeled vehicle to shock loading.

The ability to produce and measure clean, reproducible pulses suggests an immediate application in the investigation of structural attenuation and black-box isolation techniques. Various approaches have been suggested for the attenuation of shock pulses in structures. It is recommended that representative attenuation techniques and representative isolation techniques be modeled and tested to get evaluations of the techniques.

REFERENCES

1. R. F. Snell, D. C. MacKaller, and R. Guernsey, "An Electromagnetic, Plane Stress-Wave Generator," McDonnell Douglas Paper WD 1766, October 1971.

2. M. G. Pottinger, "Gage Length Effects on Strain Measurements," Instruments and Controls, September 1970, pp. 115-116.

3. H. Kolsky, "Stress Waves in Solids," Dover Publications, Inc., 1963.

4. M. Clutterbuck, "The Dependence of Stress Distribution on Elastic Constants," British Journal of Applied Physics, Vol. 9, August 1958.

5. H. Fessler and H. Lewin, "A Study of Large Strains and the Effect of Different Values of Poisson's Ratio," British Journal of Applied Physics, Vol. 11, July 1960.

6. B. Kenny, "Effect of Poisson's Ratio on Stress Distributions," The Engineer, October 30, 1964.

7. G. Murphy, "Similitude in Engineering," Roland Press, 1950, Chapter 6.

8. K. S. Valanis, "Unified Theory of Thermomechanical Behavior of Viscoelastic Materials," Published in "Mechanical Behavior of Materials Under Dynamic Loads," U.S. Lindholm Editor, Springer-Verlag, 1968.

9. J. D. Colton, and H. E. Lindberg, "Mechanical Breakup of Reentry Vehicles Under Flood and Spot Loads (U)," Vol. I: Mechanical Breakup of Reentry-Vehicle-Type Shells Under Spot Loads, (Secret) DNA-01-72-C-0062, 1972.

10. S. A. Leadbetter, H. W. Leonard, and E. J. Brock, Jr., "Design and Fabrication Considerations for a 1/10-Scale Replica Model of the Apollo/Saturn V," NASA TN D-4138, 1967.

11. P. J. Grimes, L. D. McTique, G. F. Riley, and D. I. Tilden, "Advancements in Structural Dynamic Technology Resulting from Saturn V Programs," NASA CR-1540, 1970.

TABLE 1

SUMMARY OF ACCELERATION DATA

	PHOTOELASTIC	STRAIN-GAGE	2291 ACCELEROMETER	2292 ACCELEROMETER
Acceleration (kg)	71	59	62	63
Percent of Acceleration* in Cylinder Wall	56	47	49	50
Percent of 2291 Accelerometer Reading	114	96	100	102

* Maximum acceleration in cylinder wall = 126,000 g

33
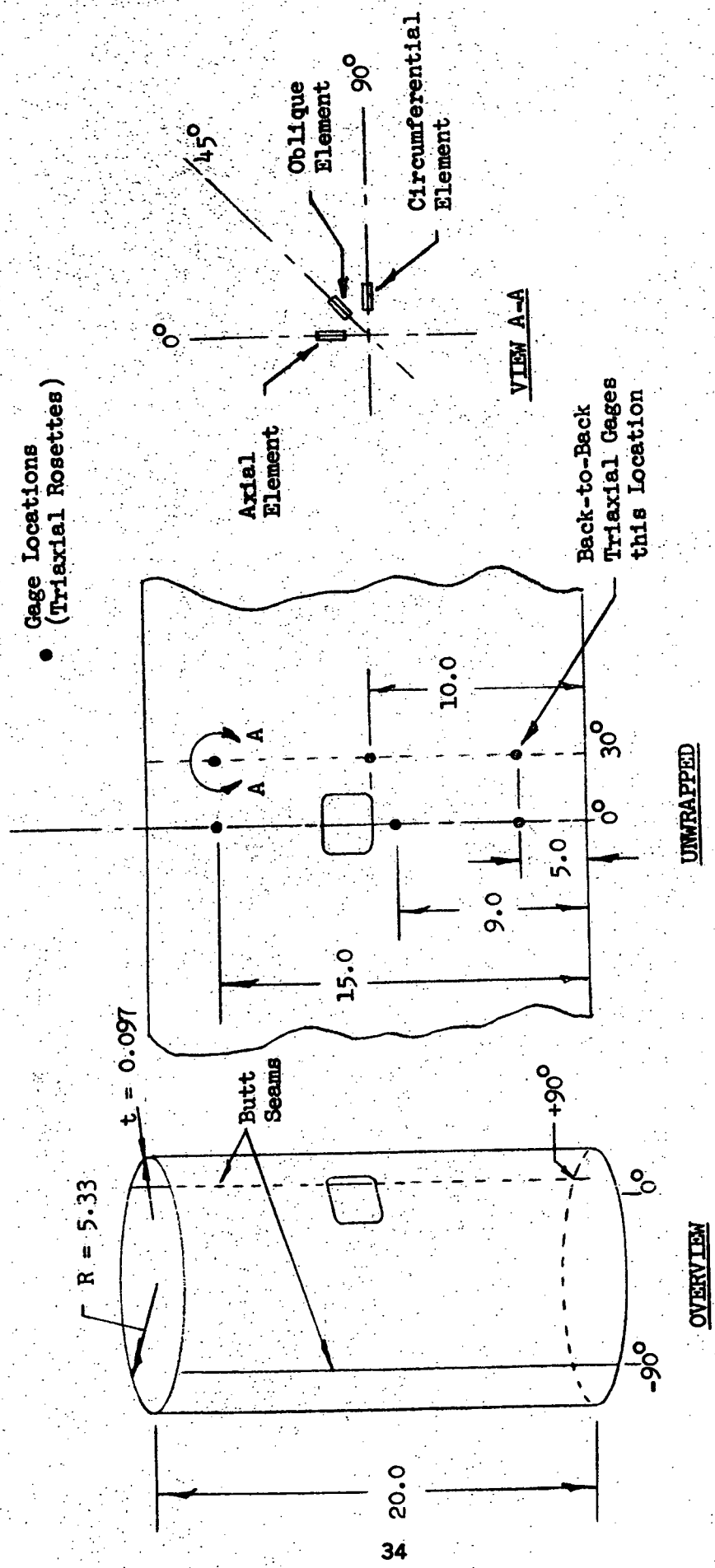
Figure 1. Configuration and Dimensions of Lexan Cylinder

34
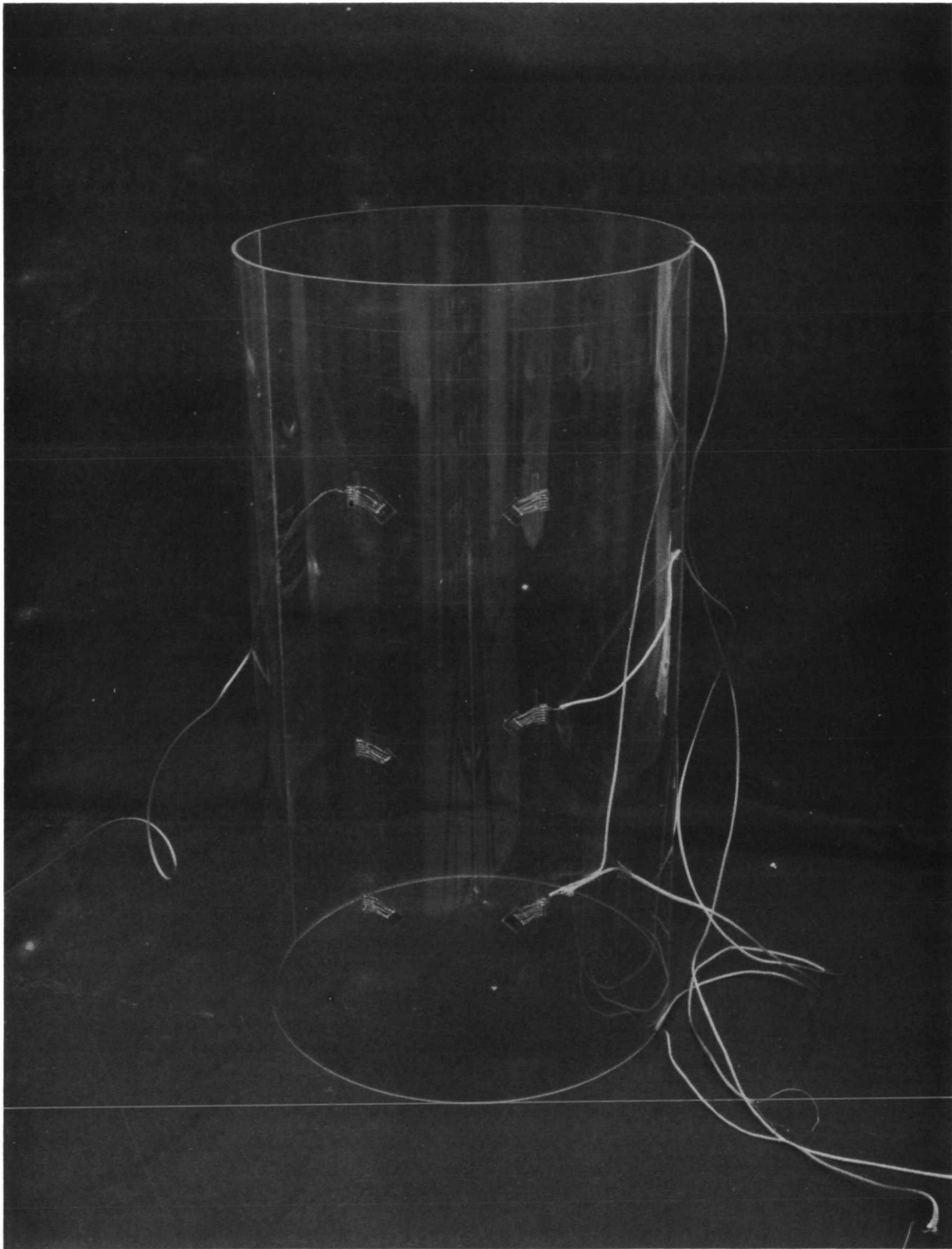
Figure 2. Lexan Cylinder with Strain Gages Attached

- Heavy arrows indicate current flow paths.
- All conducting parts are of aluminum.

0.097

0.050

0.090

VIEW A-A

Loading Strip

w = 0.25

ID = 10.50

Micarta Support Brackets

Inertial Block

-90°

+90°

4.0

A A

36
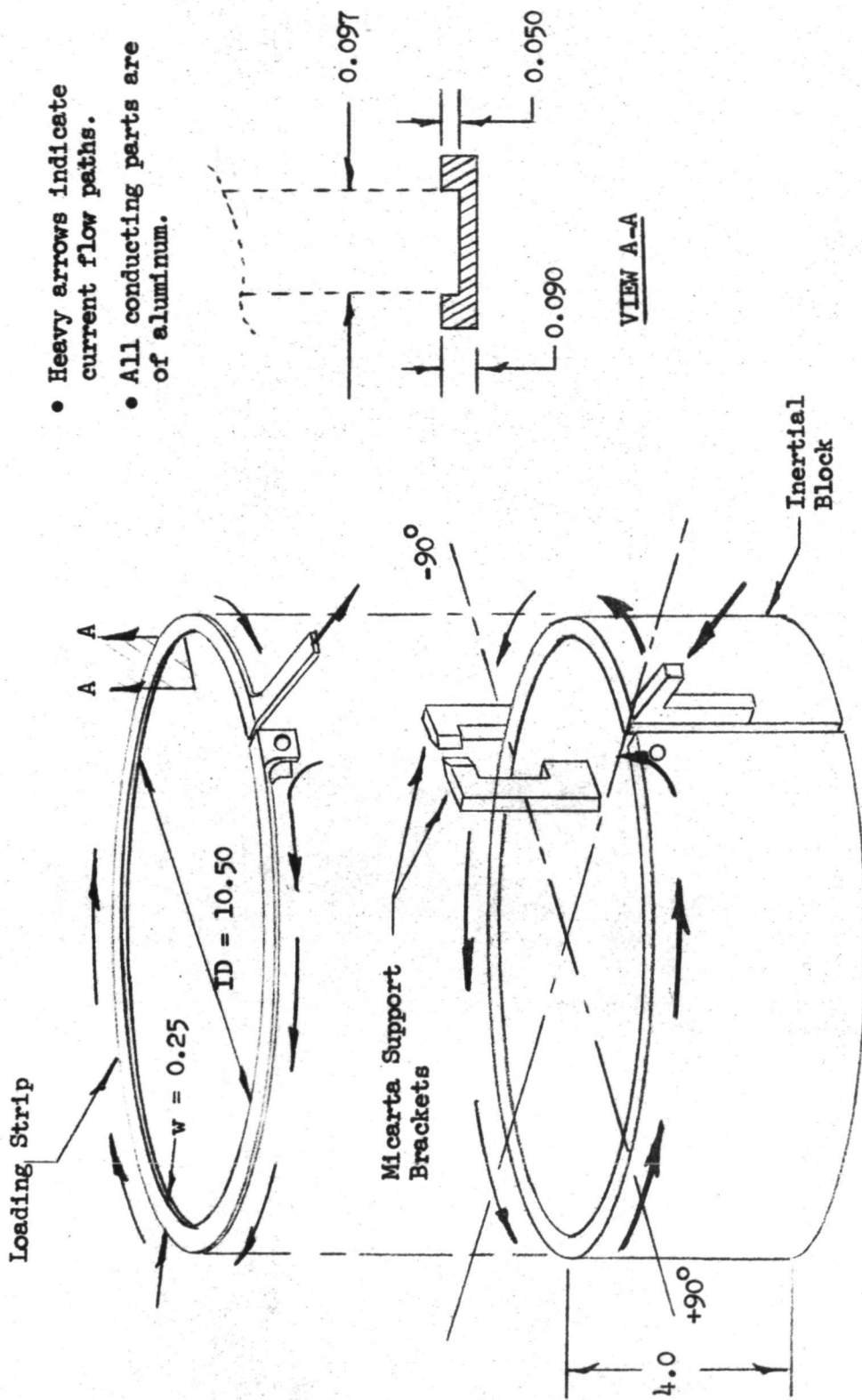
Figure 3. Loading Fixture

Figure 4. Dynamic Polariscope

- Spark-Gap Light Source
- Condensing Lenses
- Collimating Lens
- Mirror (7 x 9 Typ)
- 6-Inch Diameter Beam
- Polaroids & 1/4-Wave Plates
- Test Cylinder
- Loading Fixture
- Camera
- Monochromatic Filters
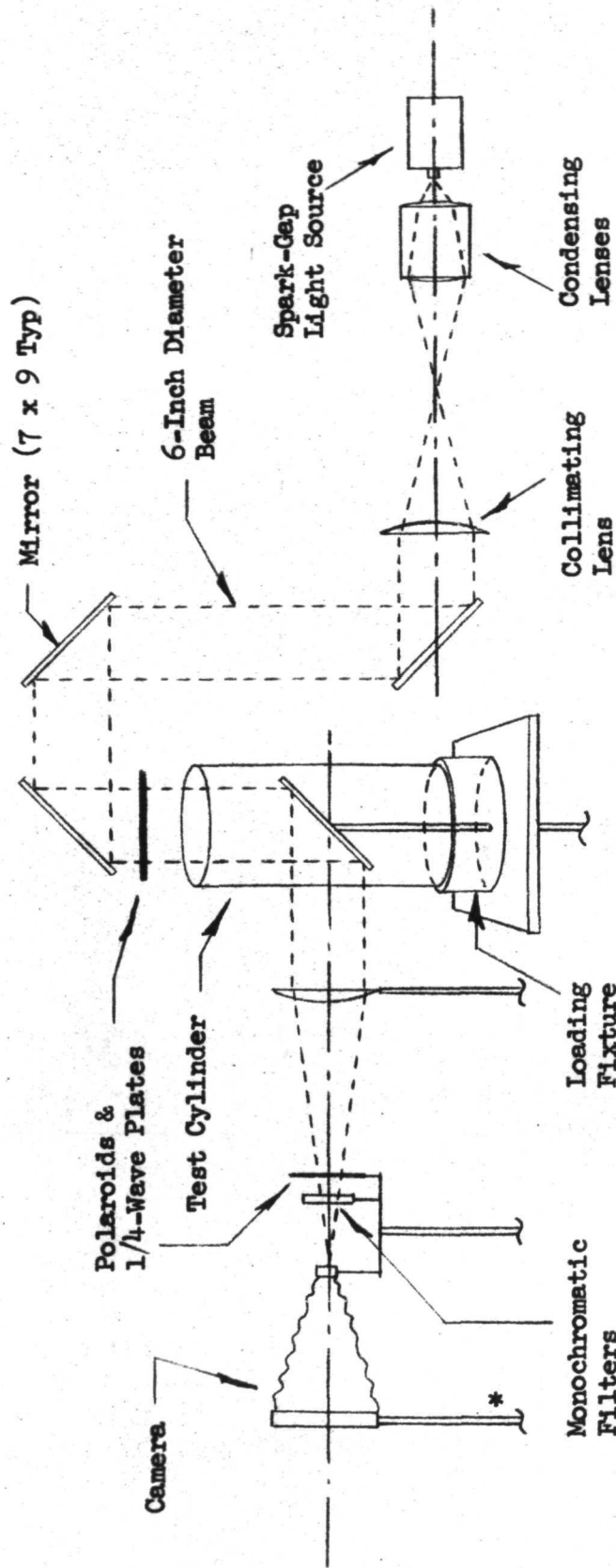
*Termination of support shafts indicate adjustibility of these shafts.

LIGHT SOURCE

LEXAN
CYLINDER

CAPACITOR
BANK

CAMERA
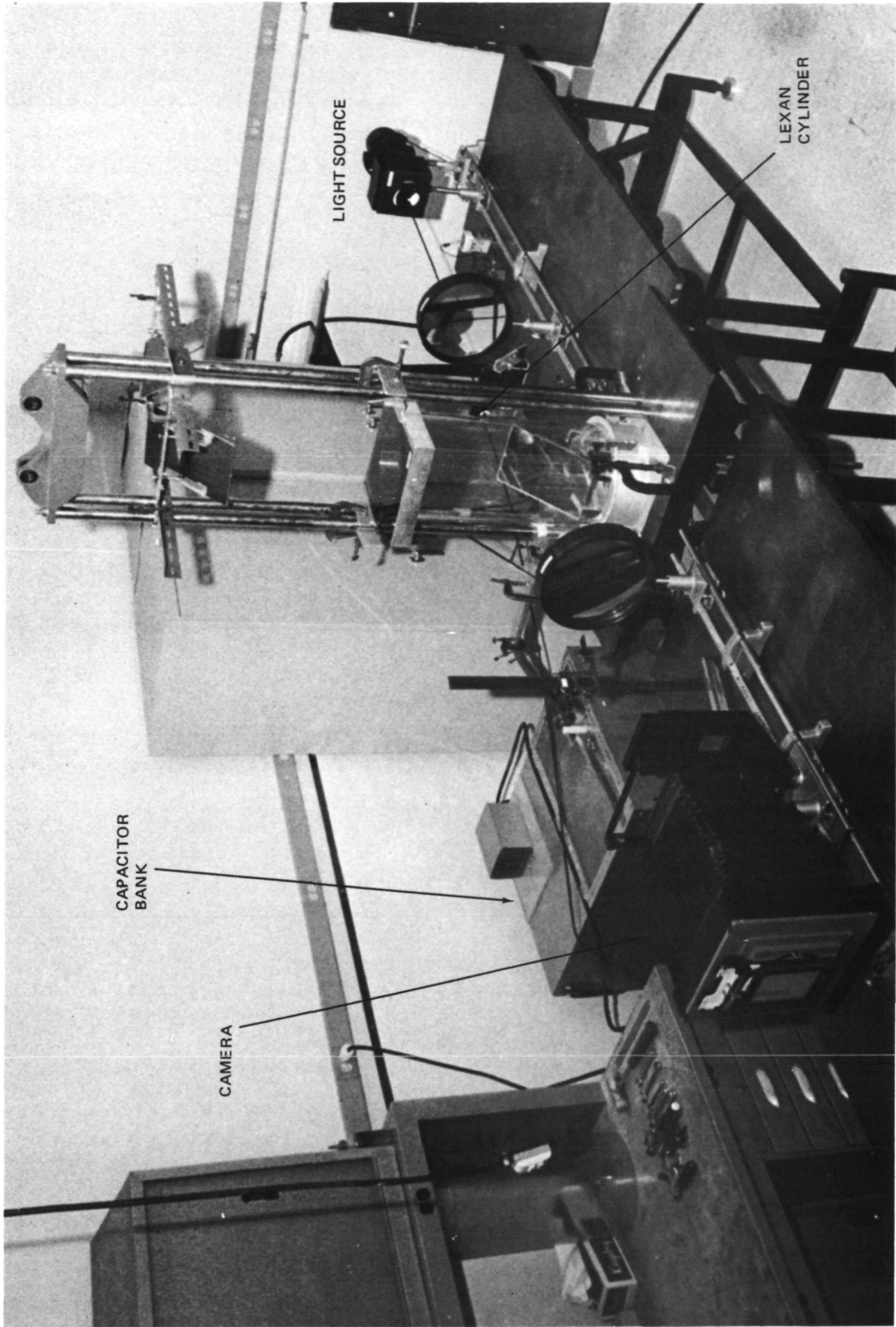
Figure 5. Test Setup

38

FRINGE ORDER

POSITION A (3— TO 8—INCH LOCATIONS)
t = 70 μSEC
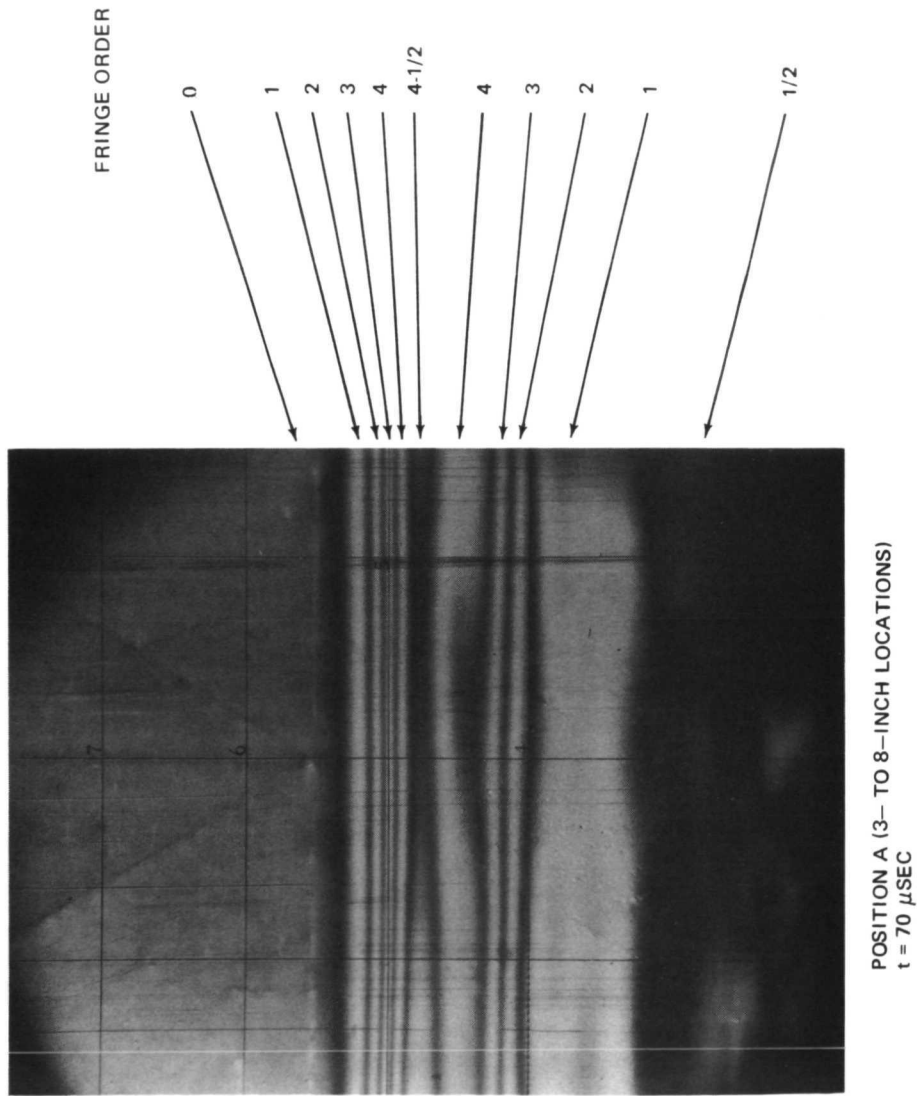
Figure 6. Typical Photoelastic Fringe Patterns of First Test Series

39

B. POSITION C (11– TO 17–INCH LOCATIONS)
t = 230 μSEC
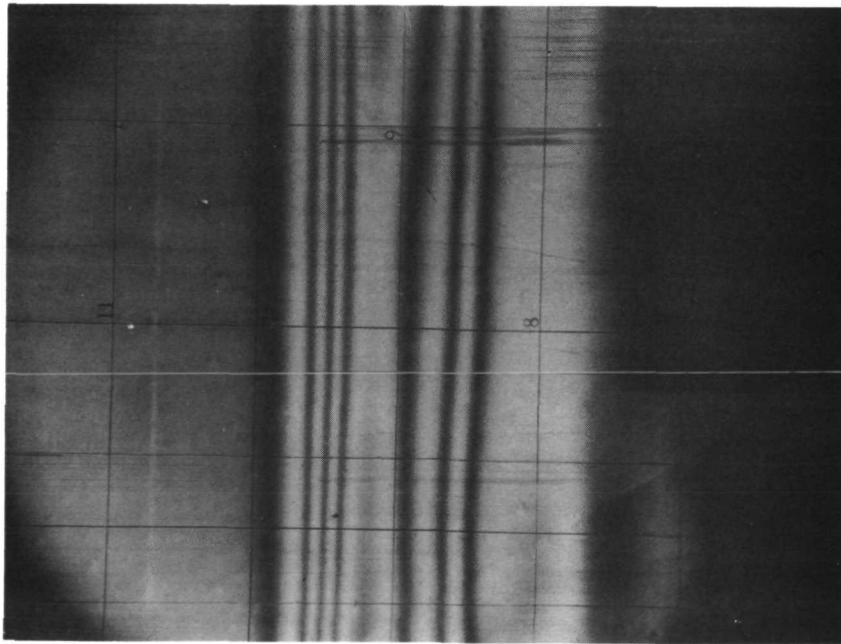
A. POSITION B (6– TO 12–INCH LOCATIONS)
t = 140 μSEC

Figure 7. Typical Photoelastic Fringe Patterns of First Test Series

40

B. t = 160 μSEC
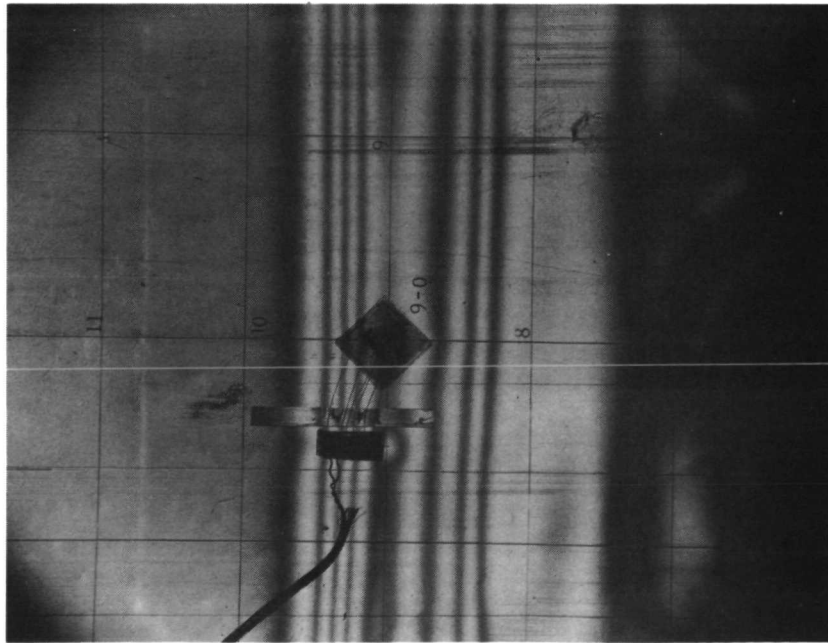
A. t = 138 μSEC

Figure 8. Photoelastic Fringe Patterns About Gage 9−0

41
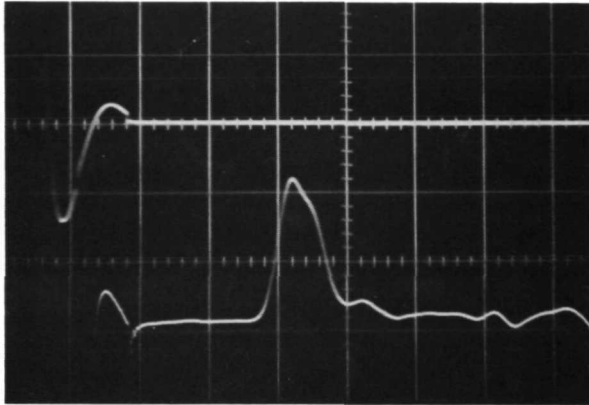
2,500 μIN./IN./CM
20 μSEC/CM
SWEEP DELAY – NONE

A. GAGE 5–0–A
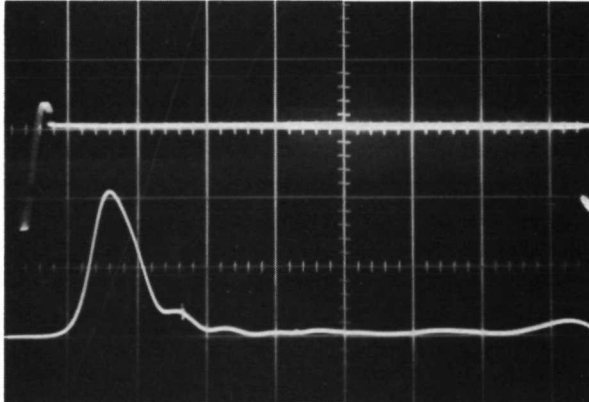
2,500 μIN./IN./CM
20 μSEC/CM
SWEEP DELAY $\approx$ 20 μSEC

B. GAGE 15–0–A

Figure 9. Strain Traces from First Test Series
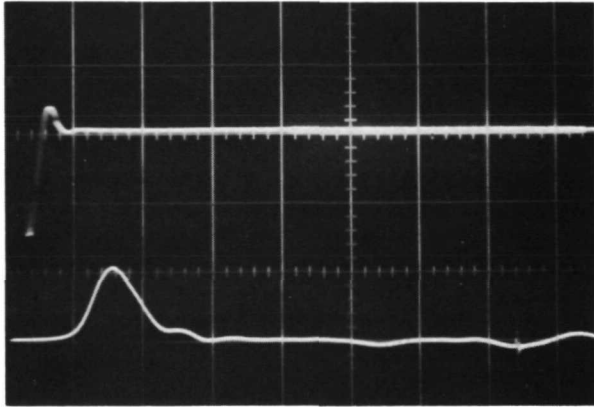
2,500 μIN./IN./CM
20 μSEC/CM
SWEEP DELAY $\approx$ 210 μSEC
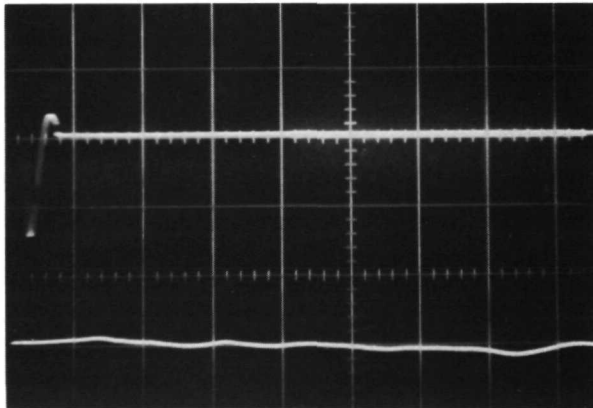
A. GAGE 15–0–0

2,500 μIN./IN./CM
20 μSEC/CM
SWEEP DELAY $\approx$ 210 μSEC

B. GAGE 15–0–T

Figure 10. Strain Traces from First Test Series

43

1.25

R = 0.50
Typ

2.00

Location of 0°
Scribe Line

10.00 to cylinder edge
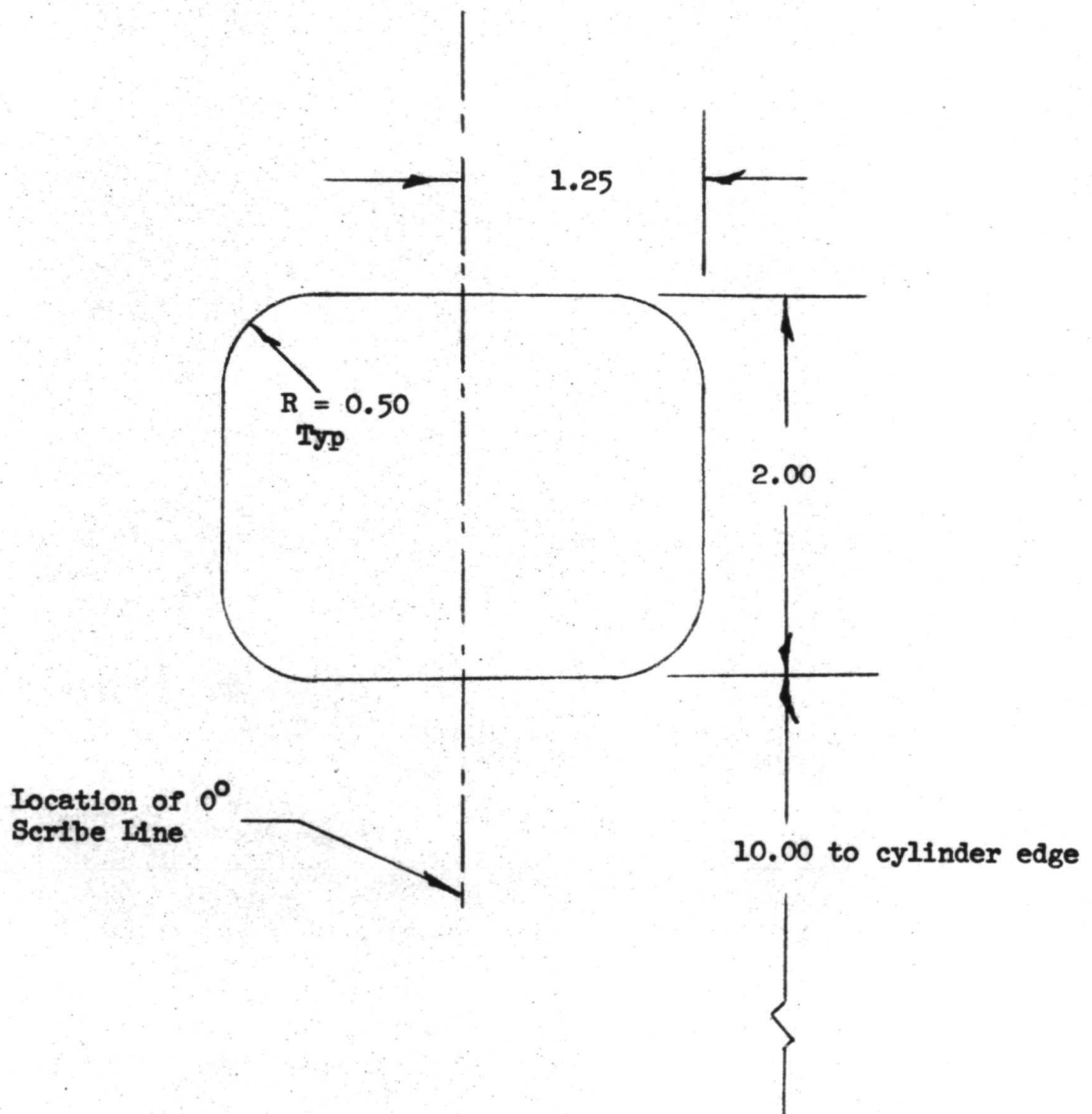
Figure 11. Dimensions of Cylinder Cutout
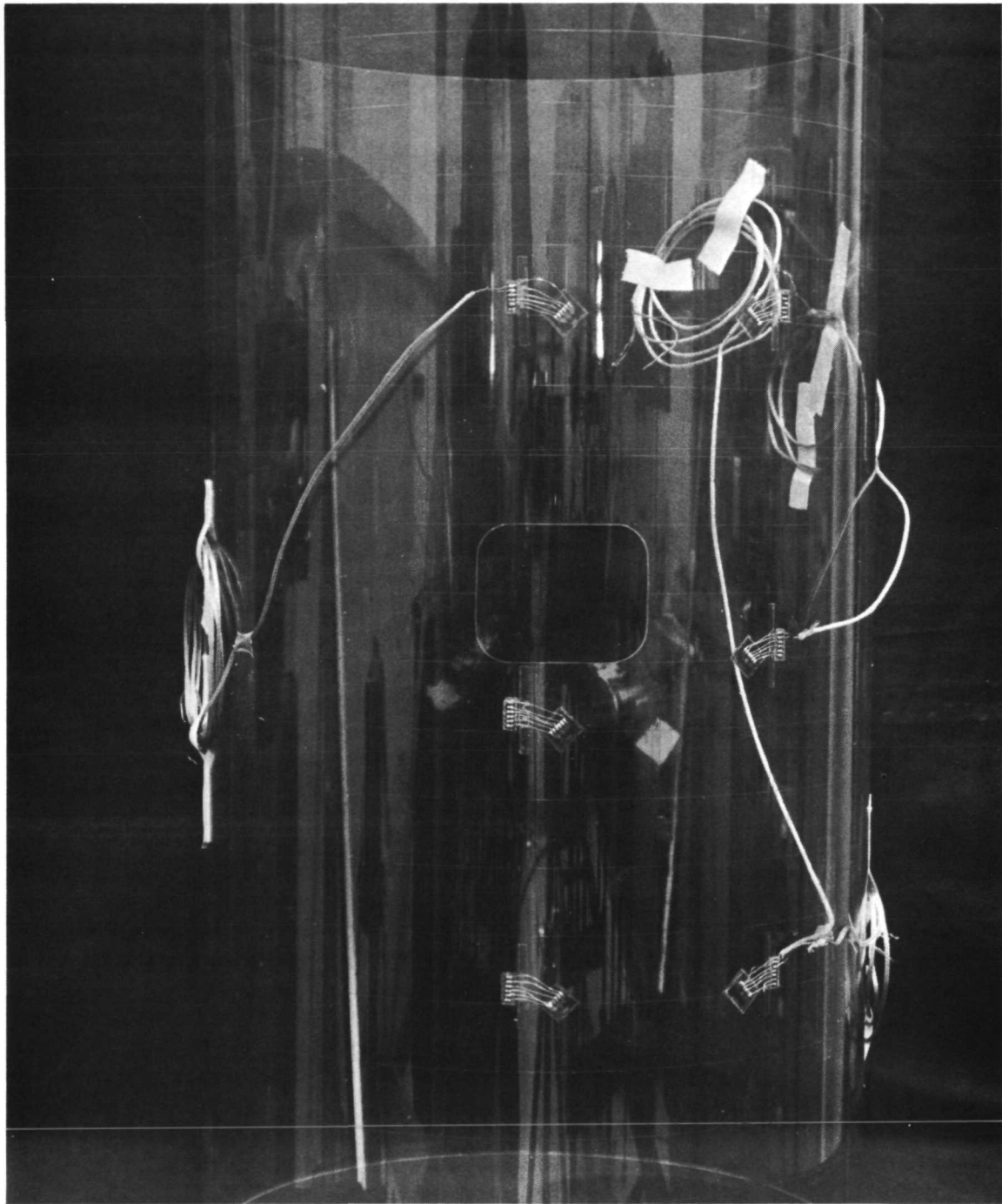
Figure 12. Cylinder with Cutout

45
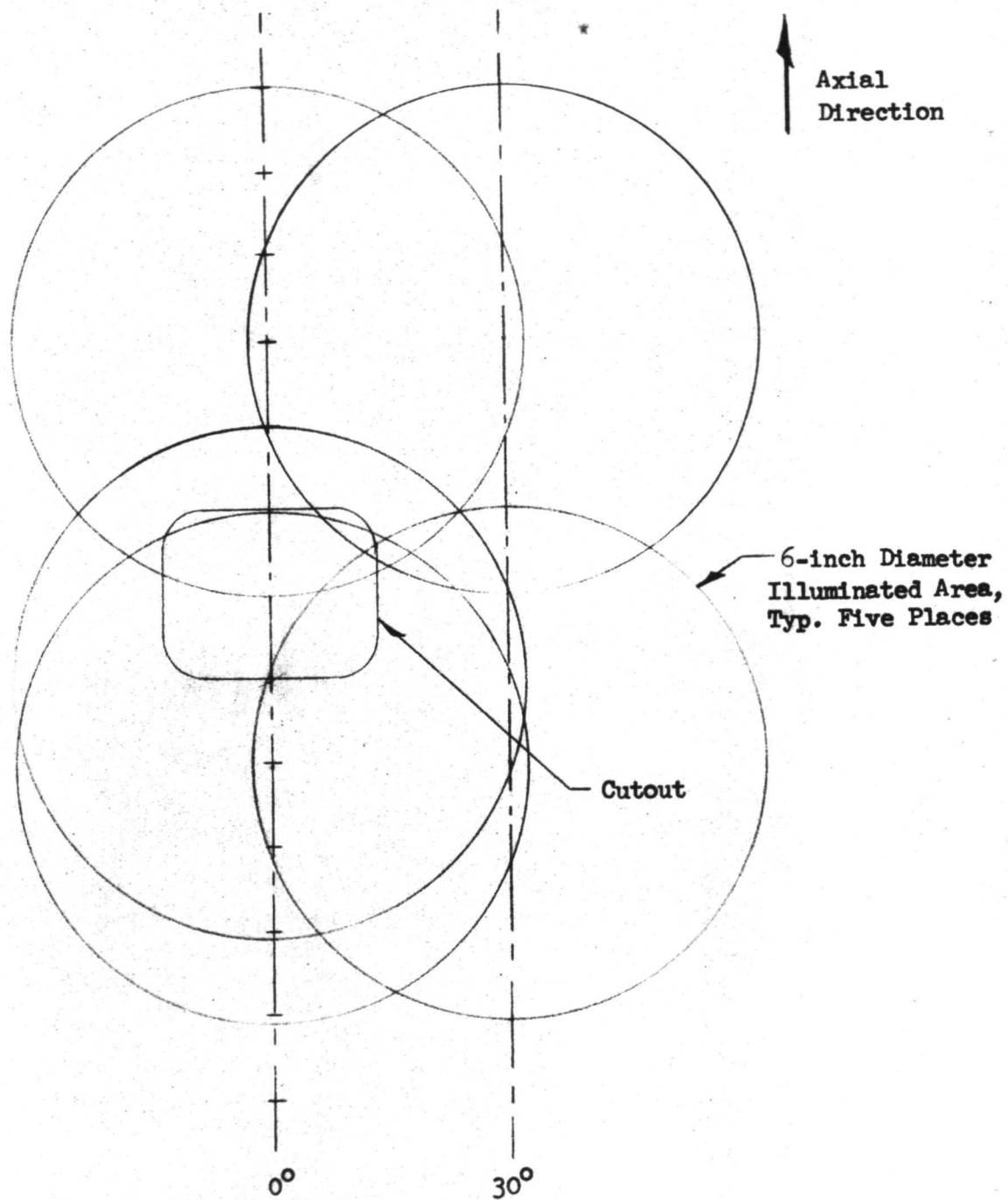
Figure 13. Illuminated Areas for Photoelastic Fringe Patterns of Second Test Series

46

B.　t = 160 μSEC
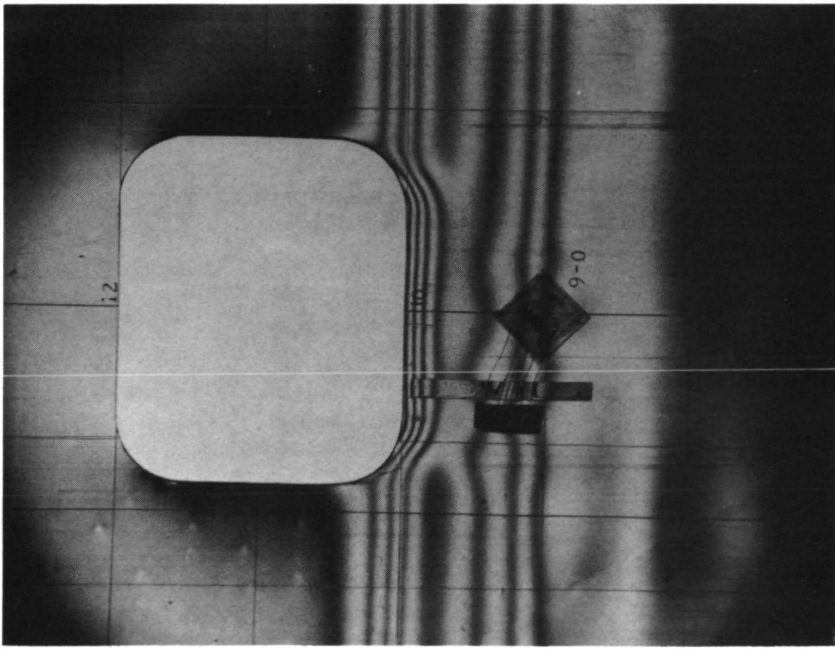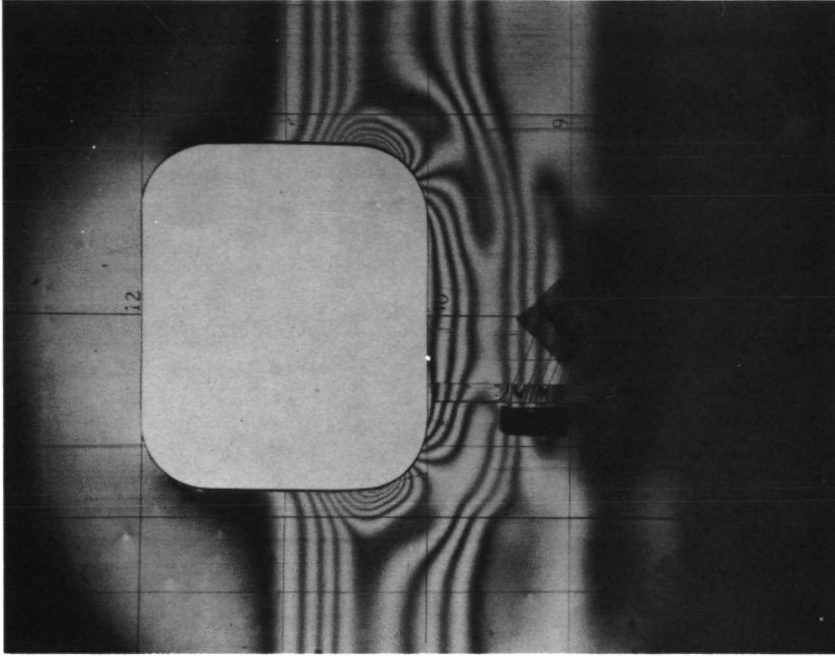
A.　t = 150 μSEC

Figure 14.　Fringe Patterns in Region of Cutout for Second Test Series

B. t = 190 μSEC
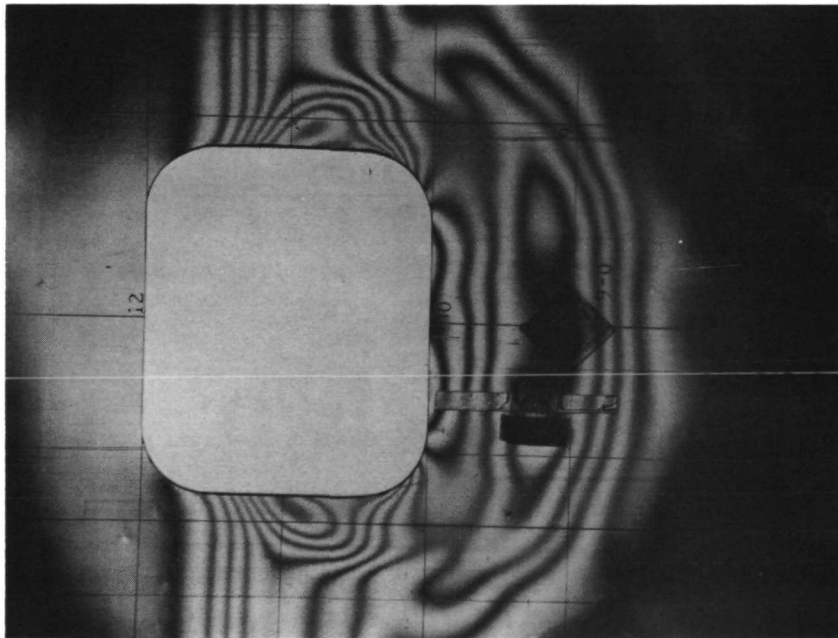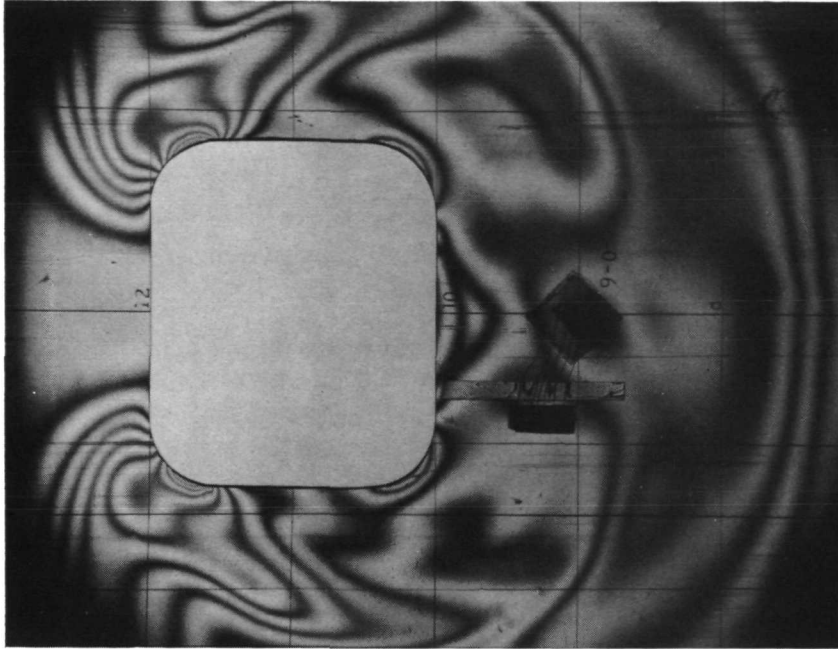
A. t = 170 μSEC

Figure 15. Fringe Patterns in Region of Cutout for Second Test Series

48

B. t = 210 μSEC
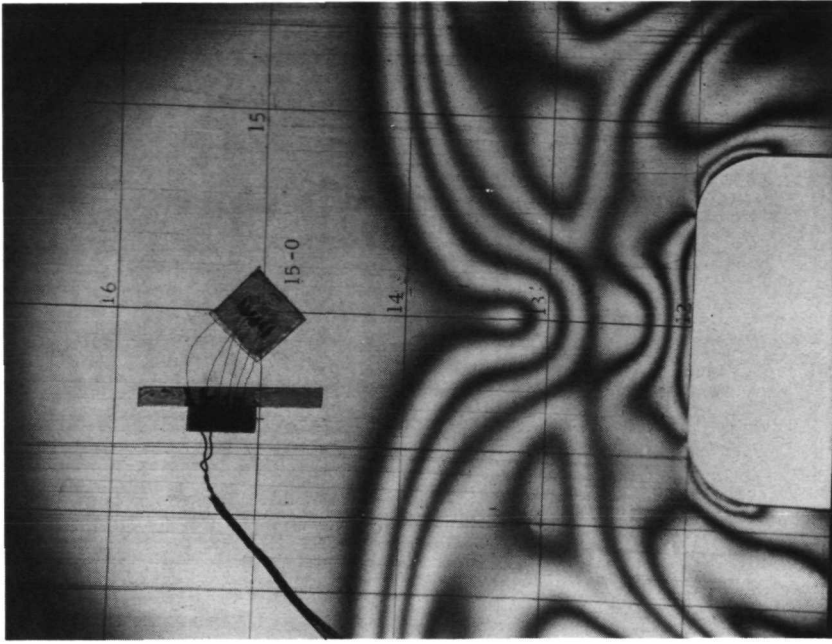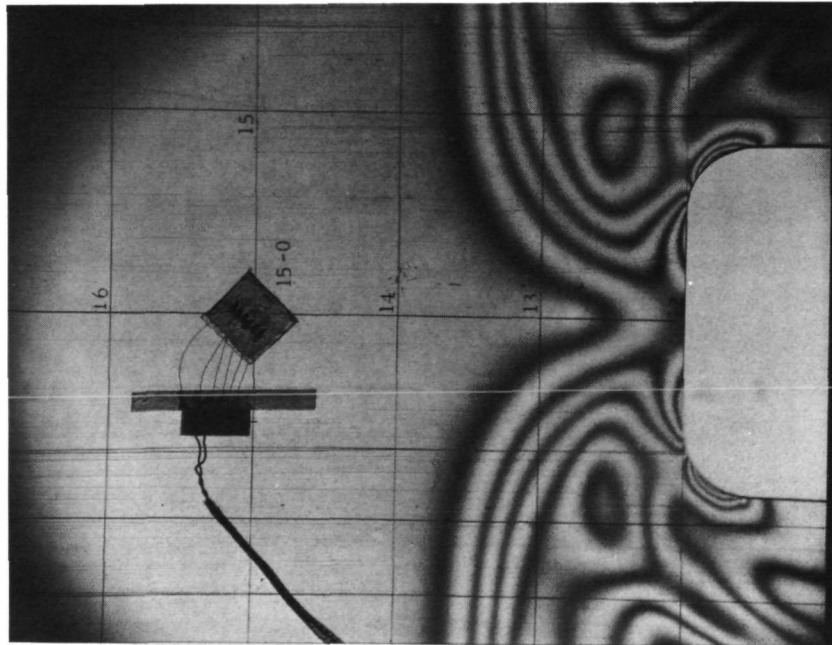
A. t = 200 μSEC

Figure 16. Fringe Patterns in Region of Cutout for Second Test Series

2,500 μ IN./IN./CM
20 μSEC/CM
SWEEP DELAY$\approx$ 20 μSEC
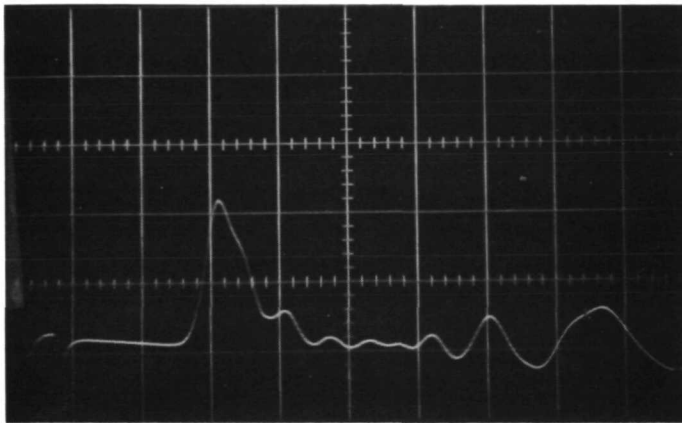
A. GAGE 5–0–A
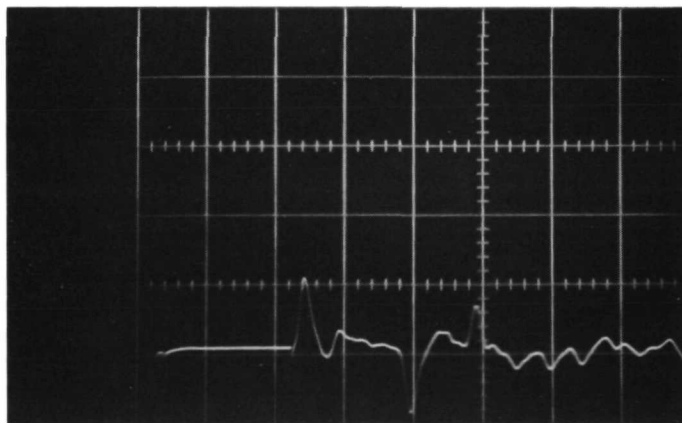
2,500 μIN./IN./CM
100 μSEC/CM
SWEEP DELAY–NONE

A   B   C
B. GAGE 15–0–A

Figure 17. Typical Strain Traces for Axial Strain-Gage Elements for Second Test Series

2,500 μIN./IN./CM
20 μSEC/CM
SWEEP DELAY $\approx$ 100 μSEC
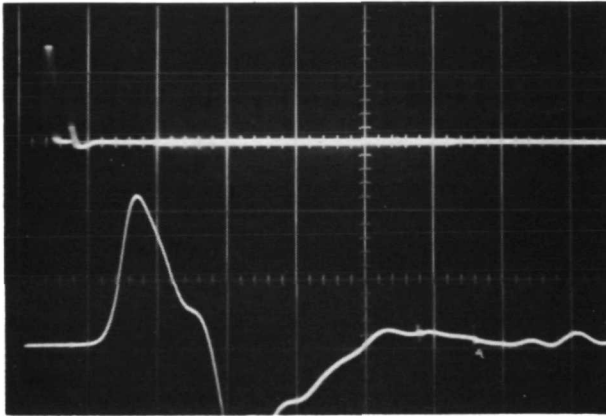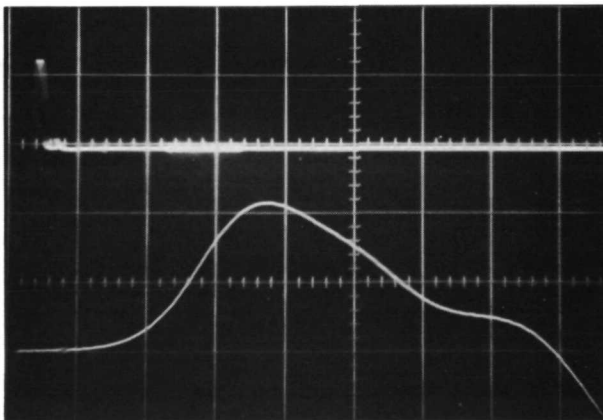
A. GAGE 9-0-A

2,500 μIN./IN./CM
5 μSEC/CM
SWEEP DELAY $\approx$ 115 μSEC

B. GAGE 9-0-A

Figure 18. Strain Traces for Axial Element of Gage 9-0 For Second Test Series
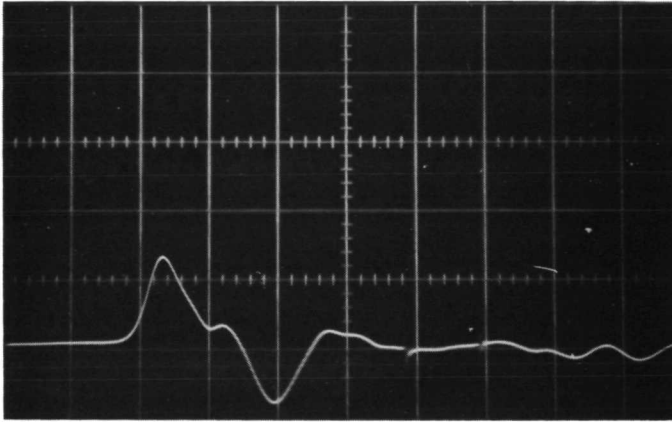
2,500 μIN./IN./CM
20 μSEC/CM
SWEEP DELAY $\approx$ 100 μSEC
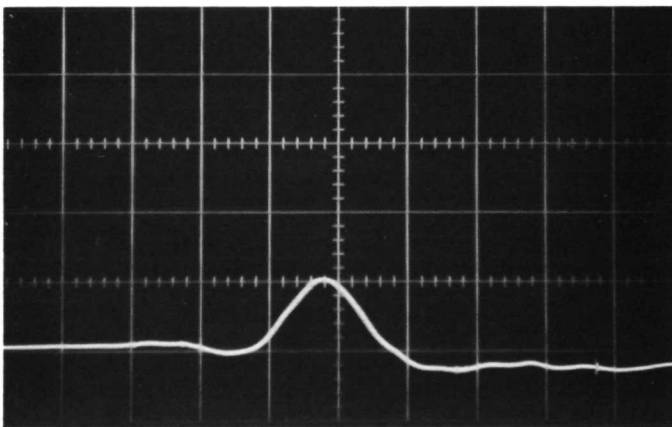
A. GAGE 9–0–0

2,500 μIN./IN./CM
20 μSEC/CM
SWEEP DELAY $\approx$ 100 μSEC

B. GAGE 9–0–T

Figure 19. Strain Traces for Oblique and Transverse Elements of Gage 9–0 for Second Test Series
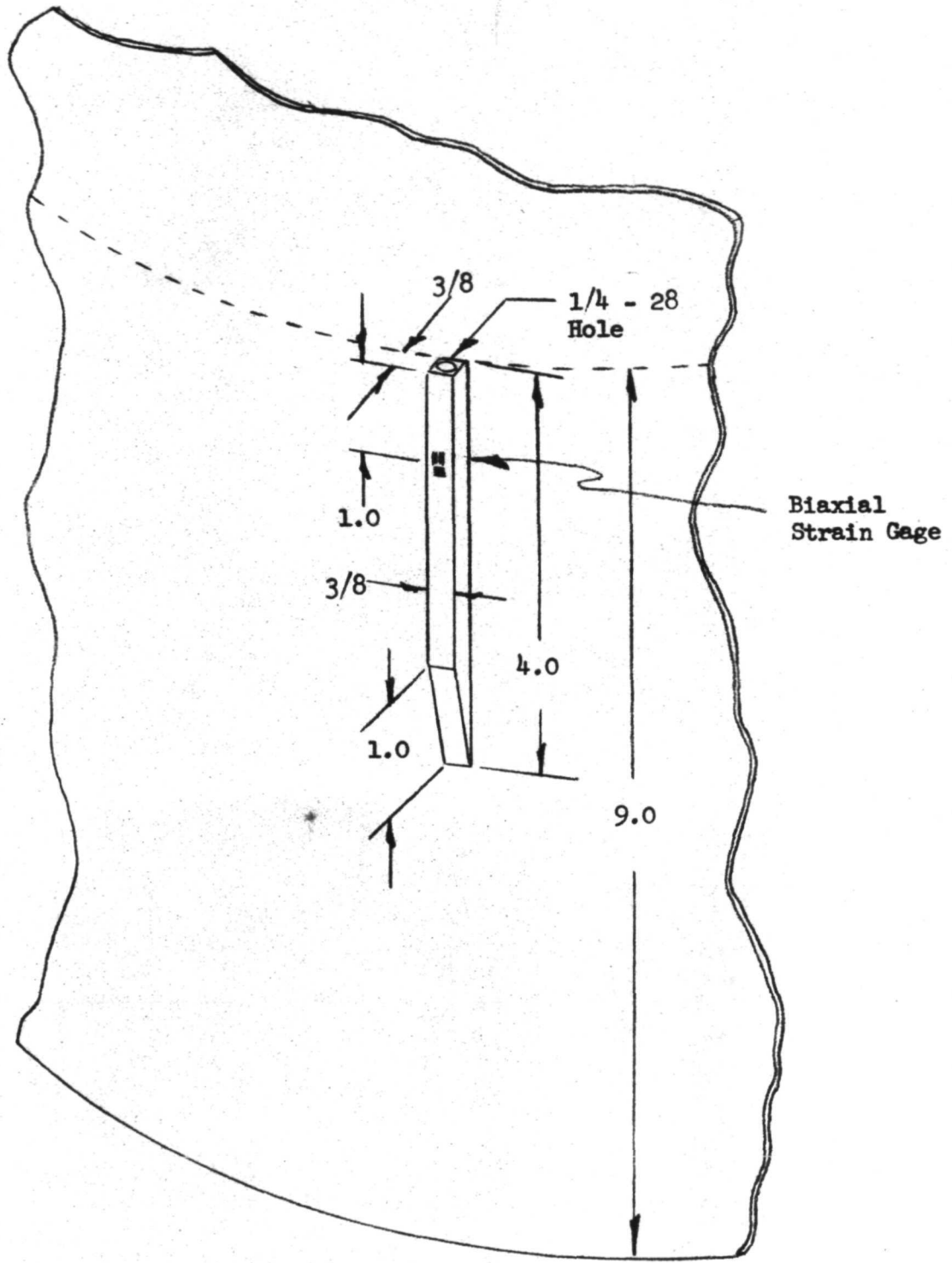
Figure 20. Dimensions and Locations of Accelerometer Mount
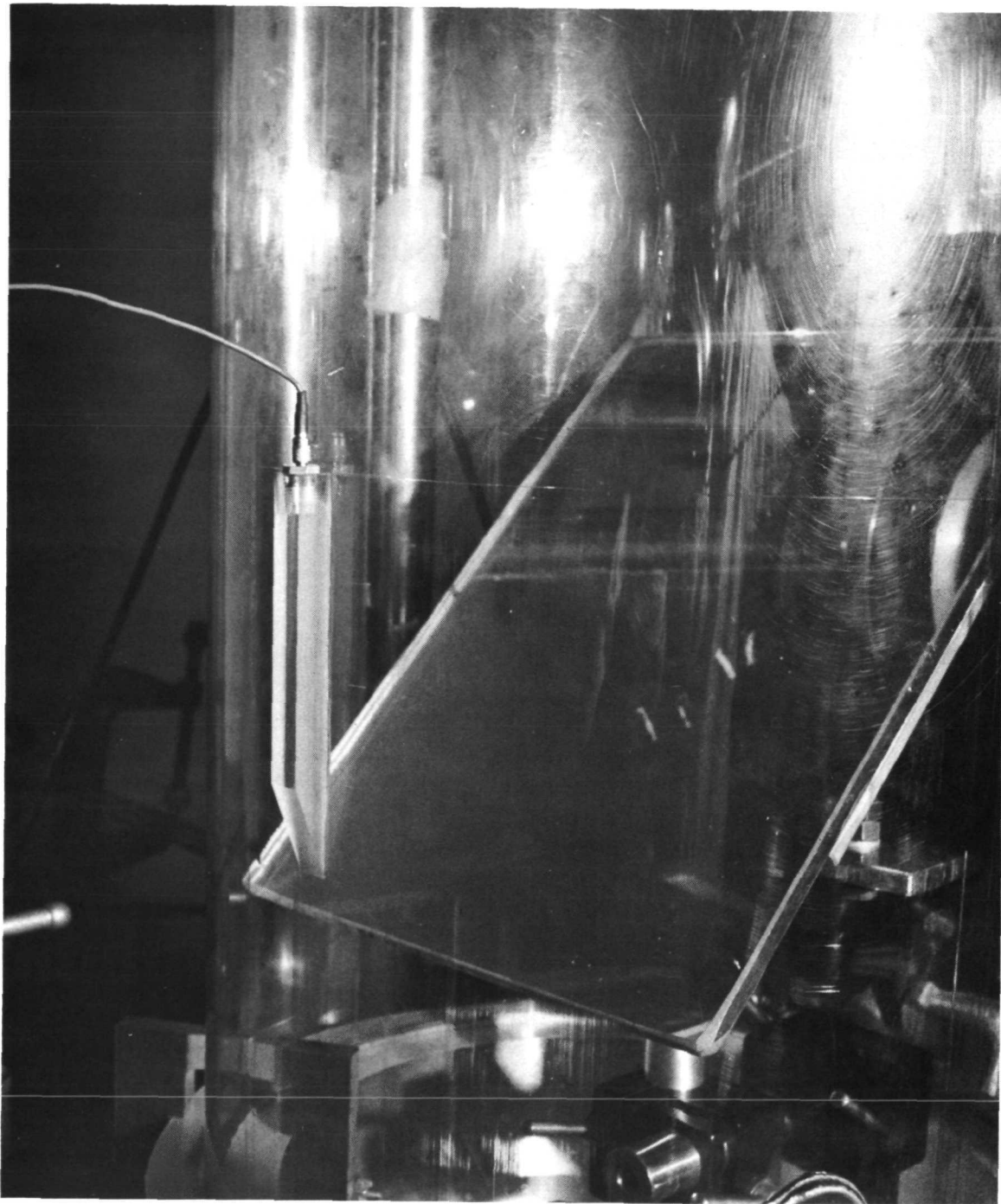
Figure 21. Accelerometer Mount with 2292 Accelerometer
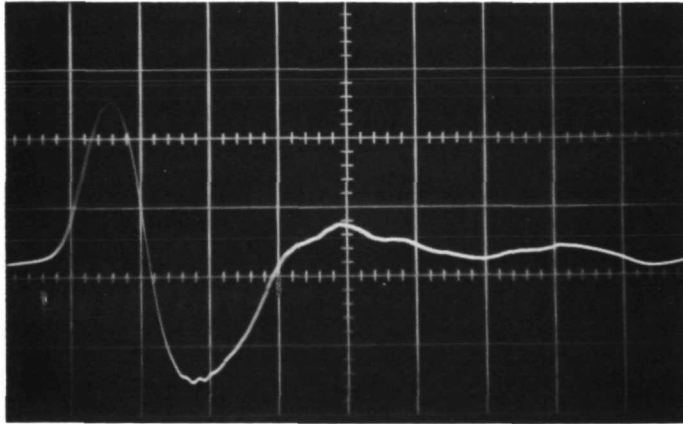
27,500 G/CM
20 μSEC/CM
SWEEP DELAY $\approx$ 120 μSEC

A. 2 291 ACCELEROMETER
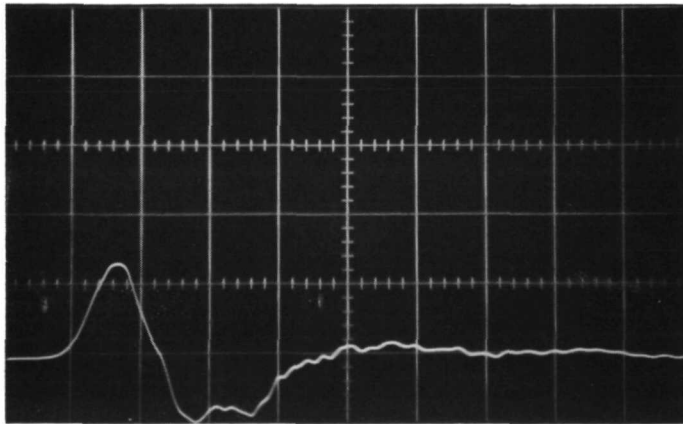
46,300 G/CM
20 μSEC/CM
SWEEP DELAY $\approx$ 120 μSEC

B. 2 292 ACCELEROMETER
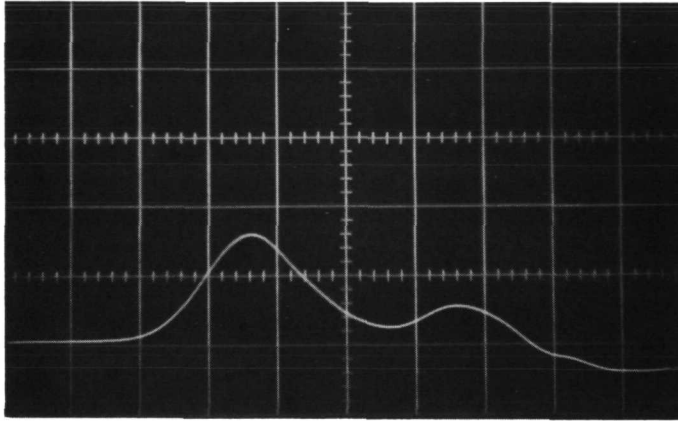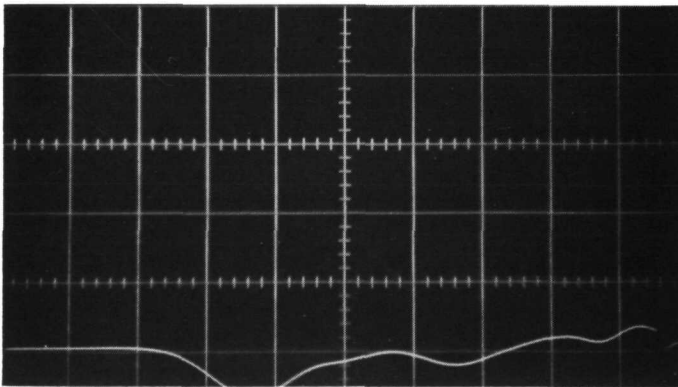
Figure 22. Accelerometer Readings in Voltage Mode
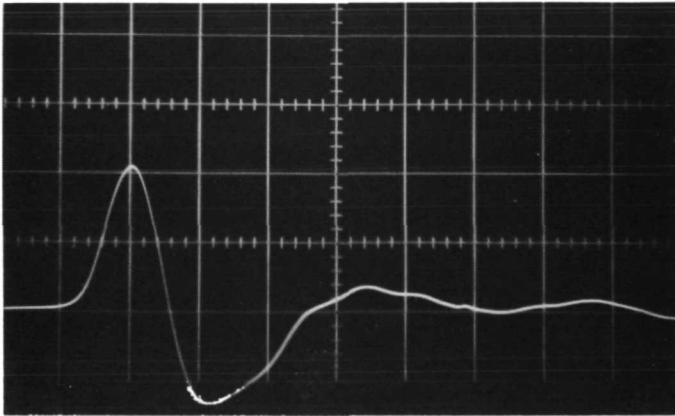
30,000 G/CM
20 μSEC/CM
SWEEP DELAY $\approx$ 120 μSEC

A.   2291 ACCELEROMETER
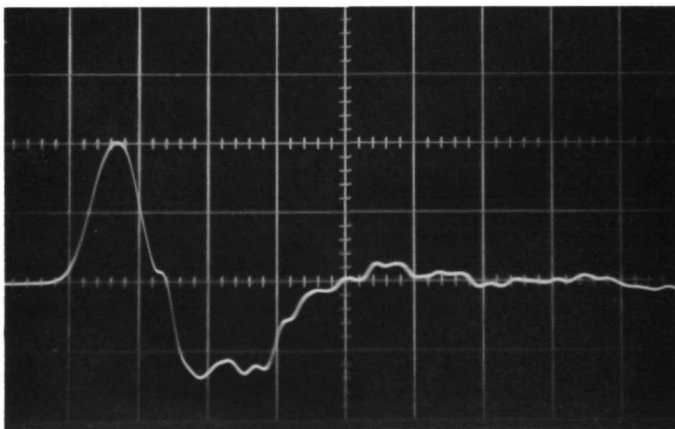
30,000 G/CM
20 μSEC/CM
SWEEP DELAY $\approx$ 120 μSEC

B.   2292 ACCELEROMETER

Figure 23. Accelerometer Readings in Charge Mode

56
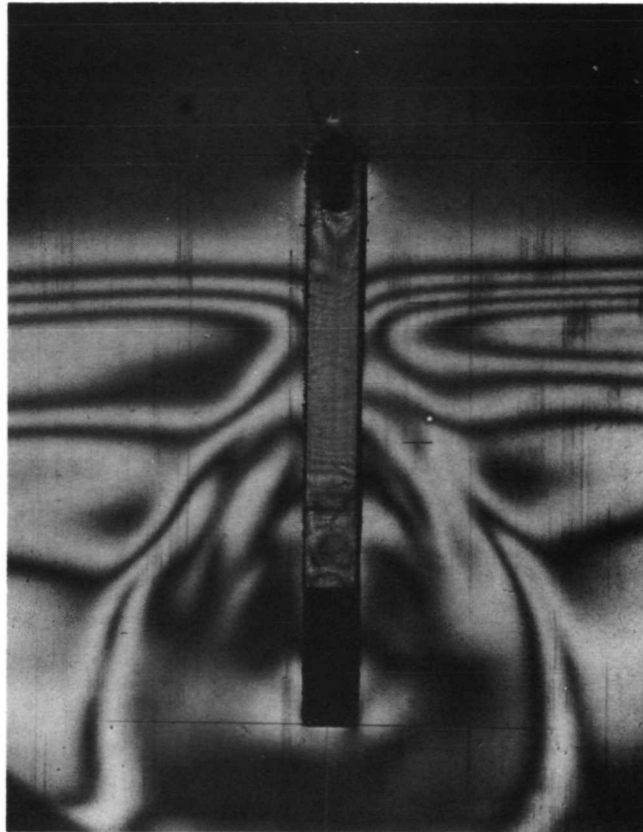
Figure 24. Photoelastic Fringe Pattern in Accelerometer Mount at t = 120 μSec

2,500 μIN./IN./CM
10 μSEC/CM
SWEEP DELAY $\approx$ 100 μSEC

A.   AXIAL ELEMENT

2,500 μIN./IN./CM
10 μSEC/CM
SWEEP DELAY $\approx$ 100 μSEC

B.   TRANSVERSE ELEMENT

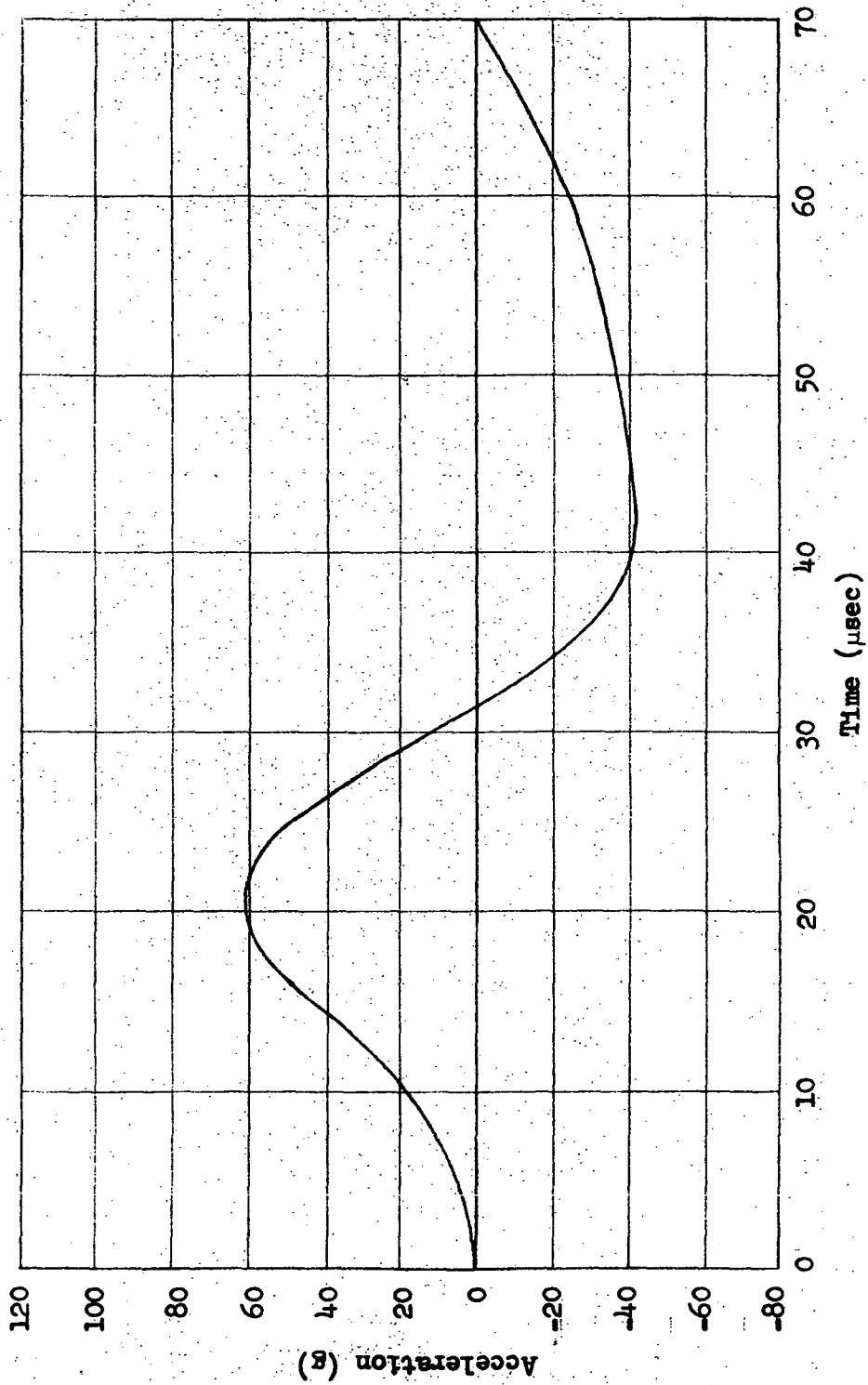Figure 25. Strain Traces from Biaxial Strain Gage Located on Accelerometer Mount

Figure 26. Acceleration History from Digitization of 2291 Accelerometer Trace
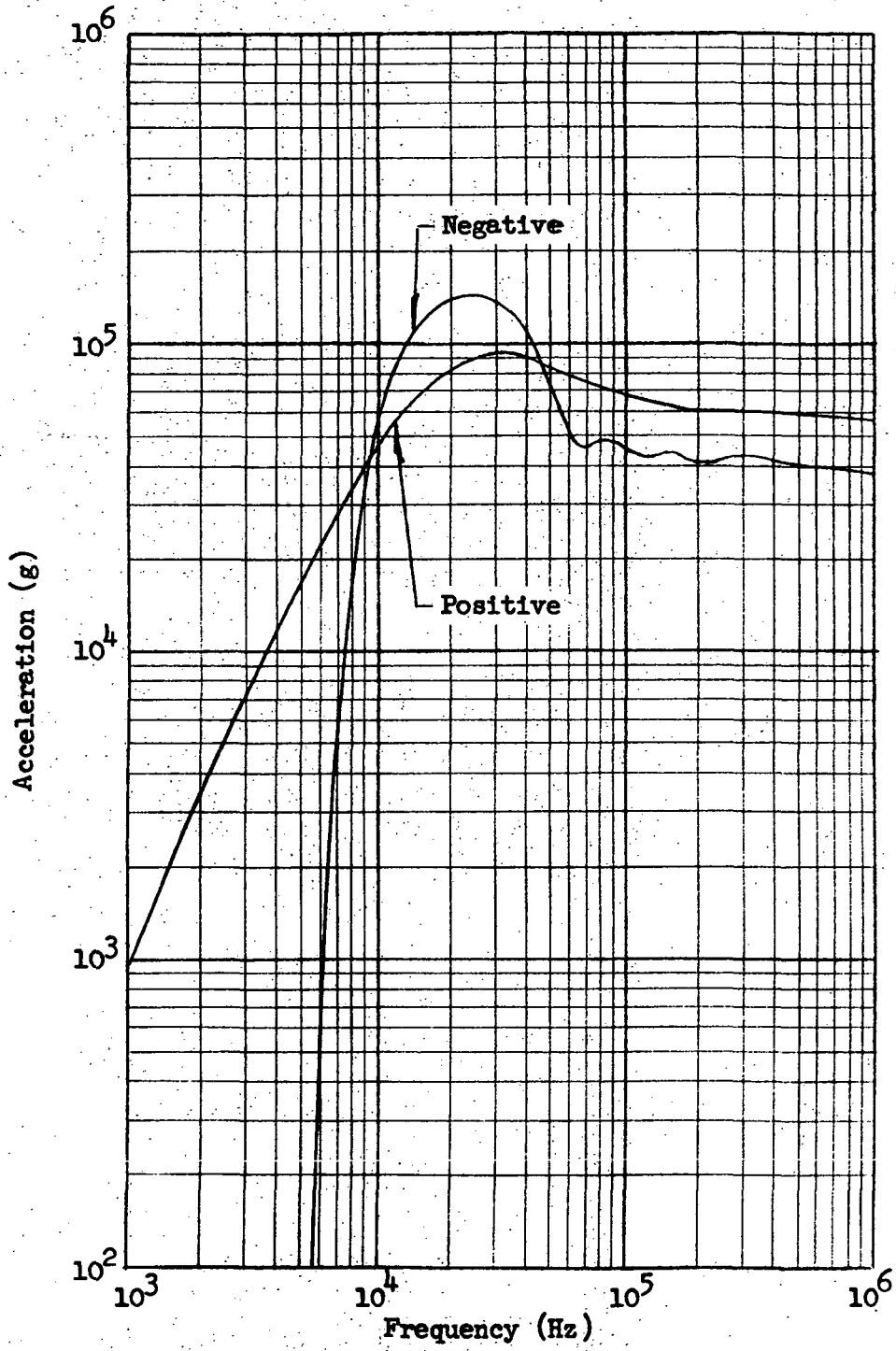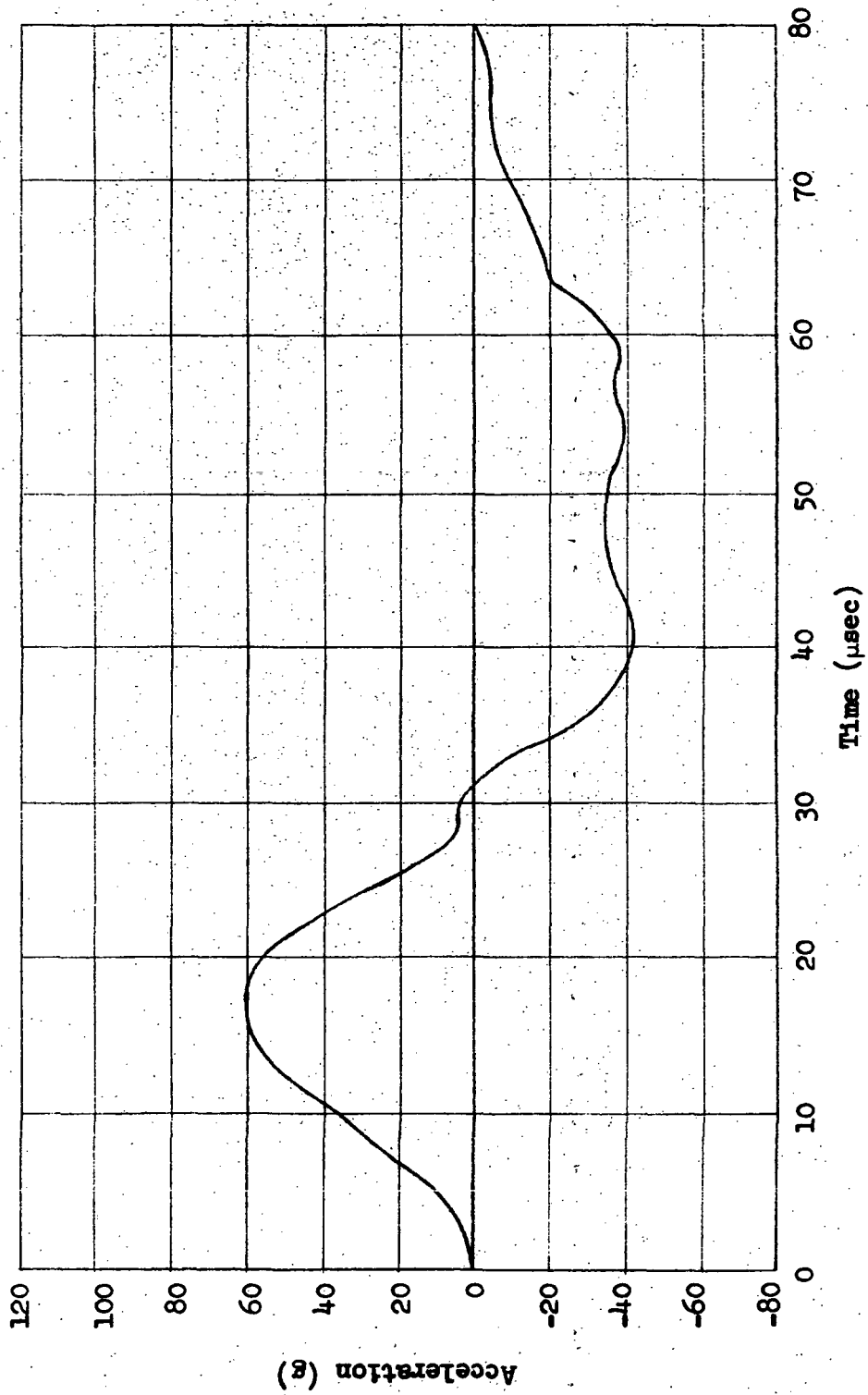
59

Figure 27. Shock Spectrum from 2291 Accelerometer Data

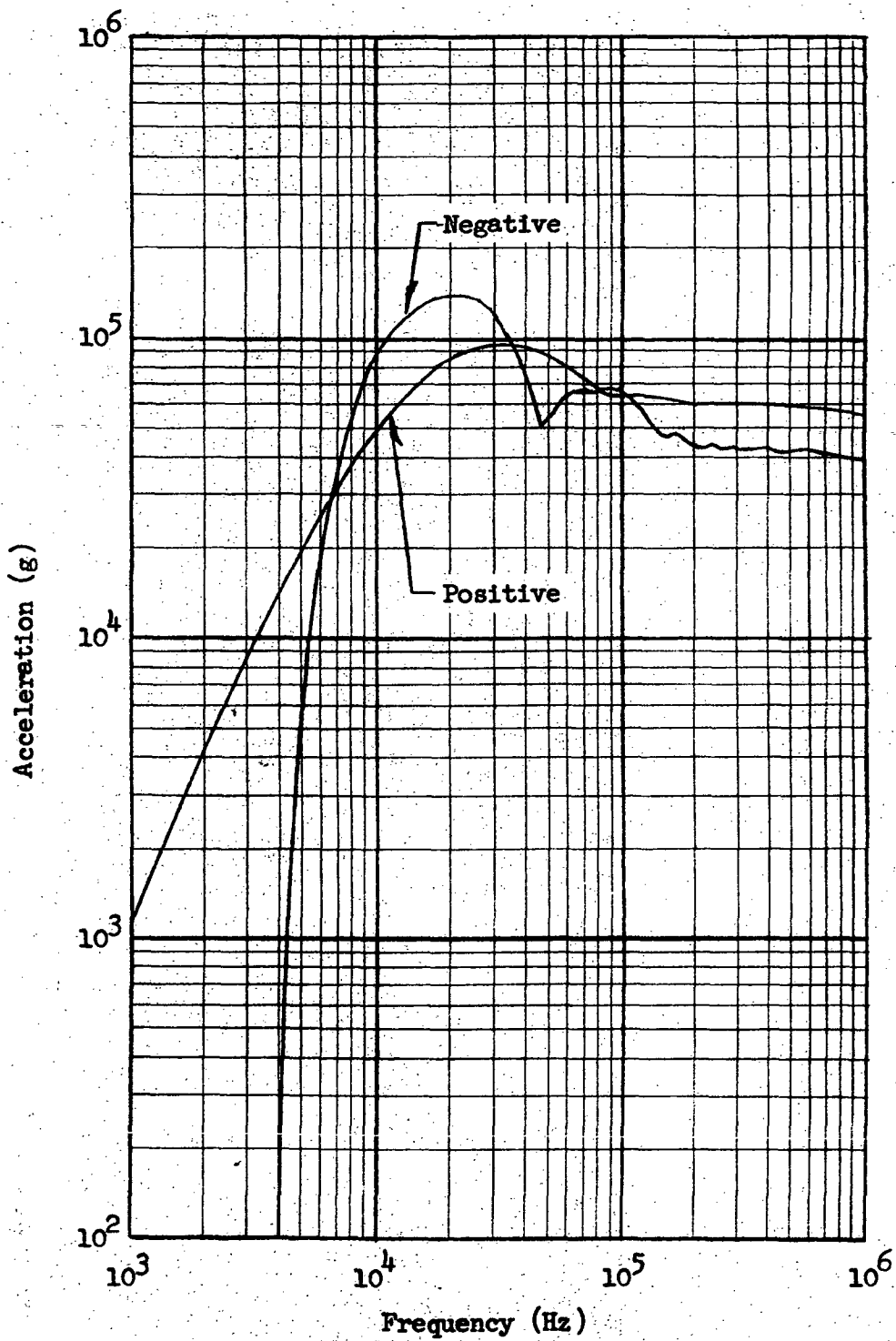Figure 28. Acceleration History from Digitization of 2292 Accelerometer Trace

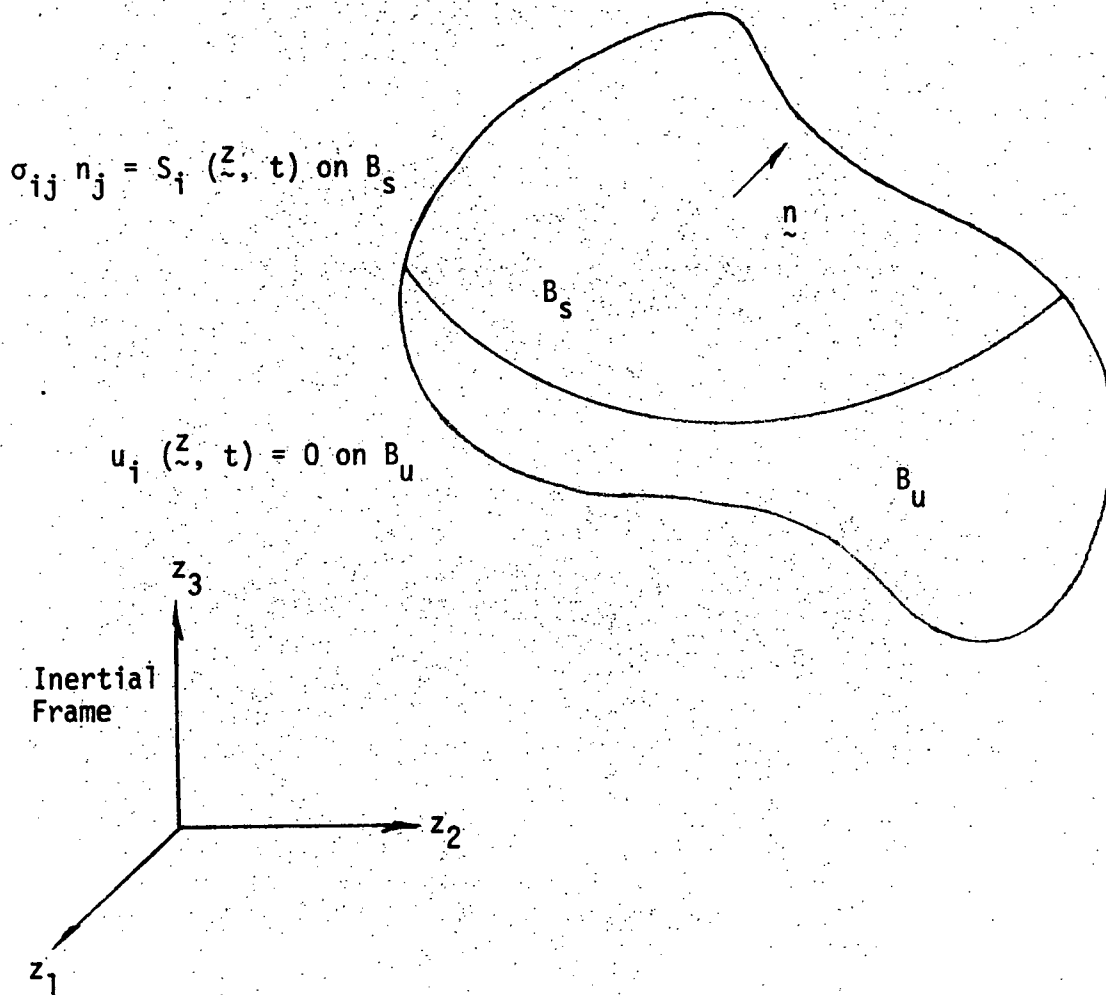Figure 29. Shock Spectrum from 2292 Accelerometer Data

$$\sigma_{ij} \, n_j = S_i \, (\underset{\sim}{Z}, \, t) \text{ on } B_s$$

$$u_i \, (\underset{\sim}{Z}, \, t) = 0 \text{ on } B_u$$

Figure 30. Elastic Body and Coordinate System

DISTRIBUTION LIST

Delivery Addressee	Number of Copies
NASA Manned Spacecraft Center R&T Space Station Procurement Section Attn: James H. Powell, Mail Code BC76(91) Houston, Texas 77058 Mark For: Contract NAS9-12873	1
NASA Manned Spacecraft Center Technical Library Branch Attn: Retha Shirkey, Mail Code JM6 Houston, Texas 77058 Mark For: Contract NAS9-12873	4
NASA Manned Spacecraft Center Management Services Division Attn: John T. Wheeler, Mail Code JM7 Houston, Texas 77058 Mark For: Contract NAS9-12873	1
NASA Manned Spacecraft Center Static and Dynamic Analysis Section Attn: D. K. McCutchen/ES24 Houston, Texas 77058 Mark For: Contract NAS9-12873	6*

* 5 copies plus 1 reproducible